DOKUZ EYLÜL UNIVERSITY
GRADUATE SCHOOL OF NATURAL AND APPLIED SCIENCES

DIRECT NUMERICAL SIMULATION OF BOUNDARY LAYER TURBULENCE

by

Gökmen YAŞAL

November, 2017
İZMİR

DIRECT NUMERICAL SIMULATION OF BOUNDARY LAYER TURBULENCE

A Thesis Submitted to the
Graduate School of Natural and Applied Sciences of Dokuz Eylül University
In Partial Fulfillment of the Requirements for the Degree of Master of Science
in Mechanical Engineering, Thermodynamics Program

by
Gökmen YAŞAL

November, 2017
İZMİR

M.Sc THESIS EXAMINATION RESULT FORM

We have read the thesis entitled **"DIRECT NUMERICAL SIMULATION OF BOUNDARY LAYER TURBULENCE"** completed by **GÖKMEN YAŞAL** under supervision of **ASSOC. PROF. DR. CAN ÖZGÜR ÇOLPAN** and we certify that in our opinion it is fully adequate, in scope and in quality, as a thesis for the degree of Master of Science.

Assoc. Prof. Dr. Can Özgür ÇOLPAN

Supervisor

Prof. Dr. M. Barış ÖZERDEM

(Jury Member)

Asst. Prof. Dr. M. Akif EZAN

(Jury Member)

Prof. Dr. Kadriye ERTEKİN

Director

Graduate School of Natural and Applied Sciences

ACKNOWLEDGMENTS

Firstly, I would like to thank my supervisors, Assoc. Prof. Dr. Can Özgür ÇOLPAN and Prof. Dr. Metin I. YARAŞ, for their encouragements, instructions, patience, advices, and supports throughout the preparation of this work. They have always been an excellent guide for me.

I would like to thank Prof. Aytunç EREK, Asst. Prof. Dr. Mehmet Akif EZAN and Prof. Mehmet Barış ÖZERDEM for their encouragements and contributions. I would also like to thank research/teaching assistant Erdoğan ALDEMİR for his helps at various critical issues in my research.

This work was aided by the support of many people. I gratefully acknowledge my friends research assistant Erdem OKUR in İzmir Economy University, Department of Software Engineering, Çağrı METİN in Dokuz Eylül University, Department of Mechanical Engineering and all my friends that I forgot writing their names, for their admirable help.

I also wish to express my particular thanks to Bestenur ÖNOL for her patience. I am also grateful for her love and tolerance in the preparation of this thesis. It was impossible to complete this thesis without her support.

Most importantly, I wish to express my gratitude to my whole family and my parents, Ercüment and Hülya YAŞAL. I am so grateful to them due to their endless support, encouragements and continual love in my whole life.

Gökmen YAŞAL

DIRECT NUMERICAL SIMULATION OF BOUNDARY LAYER TURBULENCE

ABSTRACT

In this study, the regeneration mechanism of hairpin-like coherent flow structures in transitional and turbulent boundary layers induced by the presence of riblets is investigated. According to previous studies, delaying transition the breakdown to turbulence and drag reduction by the riblets is observed compared to smooth surface. To know how the riblets change shape and dimensions of hairpin vortices will be helpful to understand how this coherent flow structures provide the effects like drag and noise reduction and delaying transition. To contribute all of these studies, a numerical study is designed that creates a turbulent spot triggered in a zero-pressure-gradient laminar boundary layer by a pulsed, transverse jet. A direct numerical simulations (DNS) is applied to observe the growth of the spot into a turbulent region. The accuracy and results of simulations are controlled by comparing the flow features over the smooth surface with the results of the previous direct numerical simulation.

Keywords: Transition, turbulent flow, riblet surface, hairpin vortices, direct numerical simulation

SINIR TABAKASI TÜRBÜLANSININ DİREKT SAYISAL SİMÜLASYONU

ÖZ

Bu çalışmada, olukların varlığı tarafından uyarılan, geçiş ve türbülanslı sınır tabakadaki firkete şekilli bağdaşık akış yapılarının yeniden üretimi araştırılmaktadır. Önceki çalışmalara göre, oluklu yüzeylerde, düz yüzeylere kıyasla türbülansa geçişin geciktiği ve sürüklenme azalımı gözlemlenmiştir. Olukların, firkete şekilli girdapların şeklini ve boyutlarını nasıl değiştirdiğini bilmek, bu bağdaşık akış yapılarının, sürüklenme, ses azalımı ve geçişin geciktirilmesi gibi etkileri nasıl sağladığının anlaşılmasına yardımcı olacaktır. Tüm bu çalışmalara katkıda bulunmak için, sıfır basınç gradyanlı laminer sınır tabakada darbeli, dik bir jet tarafından tetiklenmiş türbülans noktası oluşturan bir sayısal çalışma tasarlanmıştır. Türbülans noktasının, türbülans alanı içindeki gelişimini gözlemlemek üzere direkt (doğrudan) sayısal benzetim uygulanmıştır. Benzetimlerin doğruluğu ve sonuçları, düz yüzey için yapılan direkt sayısal benzetim sonuçları ile kontrol edilmiştir.

Anahtar Kelimeler: Geçiş, türbülanslı akış, oluklu yüzey, firkete şekilli girdaplar, direkt sayısal benzetim

CONTENTS

Page

LIST OF FIGURES

Page

LIST OF TABLES

Page

CHAPTER ONE
INTRODUCTION

1.1 Introduction

The transition of a boundary layer from laminar to turbulent state may occur via the natural or bypass mode (Morkovin, 1969). Natural transition of a boundary layer occurs in a low-disturbance environment and is characterized by viscous instability. Once triggered at a critical Reynolds number, this instability results in streamwise grouping of spanwise vorticity, thus forming the Tollmien-Schlichting (T-S) waves (Schubauer & Skramstad, 1947). The amplitude of the T-S waves initially grows linearly on a logarithmic scale as they propagate downstream (Reed et al., 1996). A secondary instability develops once the velocity perturbations due to the T-S waves reach about one to two percent of the local freestream velocity. This nonlinear phase of instability manifests itself as spanwise of periodic oscillation of the T-S waves. As the amplitude of this oscillation increases, the spanwise vorticity of the boundary layer develops a streamwise component, thereby initiating self-induced motions in the wall-normal direction. In the presence of the wall-normal velocity gradient of the undisturbed boundary layer, such induced motions result in local stretching of the T-S waves, thereby forming Λ-shaped vortical structures that assume the shape of a hairpin upon further stretching, as shown in Figure 1.1.

A simplified description of the local flow field associated with a hairpin vortex is that the upwash and downwash motions primarily induced by the streamwise legs of the hairpin vortex result in wall-normal redistribution of streamwise mass flow. This creates a streaky pattern in the streamwise velocity field, with high-speed streaks located on the outboard sides of the hairpin vortex closer to the wall, and a low speed streak located between the leg of the hairpin vortex, and at a relatively greater distance from the wall (Schröder & Kompenhans, 2004; Yaras, 2007).

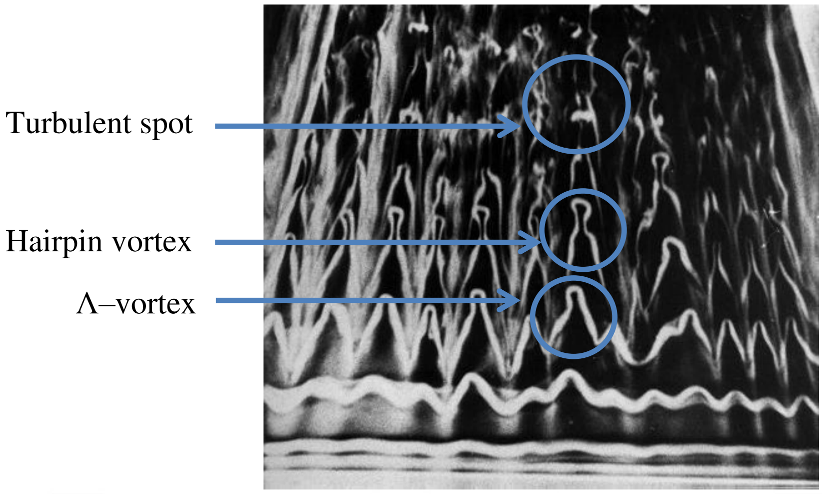

Figure 1.1 Smoke-wire visualizations of Λ-vortices, hairpin-vortices, and turbulent spots (Adapted from Perry et al., 1981)

The shear layer surrounding each streak has a streamwise velocity profile with an inflection point, as such is inviscid unstable (Swearingen & Blackwelder, 1987). The instability manifests itself in one of two modes referred to as the sinuous and varicose modes. In instances where the perturbation velocity of the streak is less than about 26% of the local free-stream velocity, the sinuous mode is more likely; otherwise, the varicose mode tends to dominate (Elofsson et al., 1999; Brandt & Henningson, 2002).

The instability of the shear layer surrounding a streak results in streamwise periodic grouping of the vorticity contained within the shear layer, in a manner akin to the developments leading to the formation of T-S waves in laminar boundary layers, eventually resulting in the formation of several new hairpin vortices that are approximately aligned in the streamwise direction. This train of hairpin vortices constitutes a wavepacket. There are two possible generation and growth mechanisms of these coherent structures; one involving the newly formed hairpin vortices straddling the nearest leg of the parent hairpin vortex (Schröder & Kompenhas, 2004); the other involving newly formed hairpin vortices developing between the

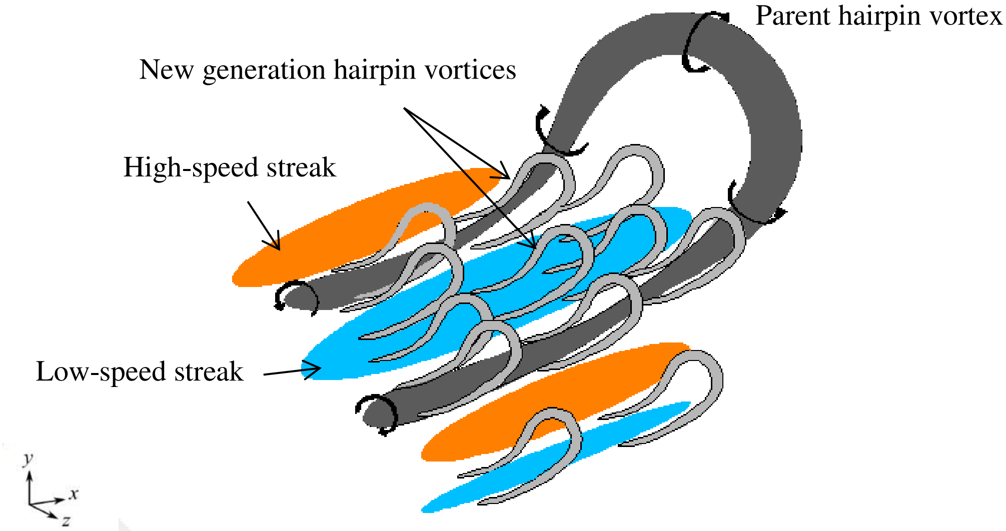

Figure 1.2 Mechanisms leading to longitudinal and lateral growth of a wavepacket

legs of the parent hairpin vortices (Singer and Joslin, 1994). When the legs of parent hairpin vortex are not closely spaced in the spanwise direction, child hairpin vortices straddle the nearest leg of the parent hairpin vortex. This mechanism is observed frequently among the larger-scale hairpin vortices residing near the leading edge and spanwise edge of a turbulent spot. However, when the legs of the parent hairpin vortex are closely spaced, the child hairpin vortices tend to form between these legs, and this mechanism is observed among smaller-scale hairpin vortices which typically prevail near the trailing-edge of the turbulent spot (Brinkerhoff & Yaras, 2014). The process of creation of a wavepacket is schematically illustrated in Figure 1.2. The main factor affecting the number of hairpin vortices within a wavepacket is the Reynolds number based on the local freestream velocity and displacement thickness of the boundary layer, $Re_{\delta*}$. A wavepacket tends to contain two to three hairpin vortices at $Re_{\delta*}$ values of the order of 100, with this count reaching five for $Re_{\delta*}$ values of the order 1000 (Adrian et al., 2000). The streamwise spacing between the hairpin vortices in a wavepacket in a zero-pressure-gradient boundary layer is several hundred viscous wall units (Adrian et al., 2000). The spanwise spacing between adjacent wavepackets varies from 60 to 180 wall-units with a mean value of 100 viscous wall units (Adrian et al., 2000; Smith & Metzler, 1983; Kline et al., 1967).

Here, the viscous wall-unit refers to the length scale based on the kinematic viscosity and friction velocity at the nearest wall. In the presence of favourable streamwise pressure gradient, the spanwise spacing between wavepackets is two to three time larger than for zero-pressure-gradient boundary layers (Yaras, 2007).

As the wavepacket convects in the downstream direction, the hairpin vortices within it grow through stretching and entrainment mechanisms, and eventually spawn new wavepackets through the same mechanism through which they were created. Multiple occurrences of this evolutionary pattern results in the coexistence of several generations of wavepackets in a mature region of turbulence, where the younger wavepackets may be partially or completely immersed in older ones (Brinkerhoff & Yaras, 2014). Mutual interaction of wavepackets of mutiple generations results in a complex three dimensional and transient flow field, where the original vortical structures that initially resembled hairpin vortices assume a broad range of shapes including symmetric, asymmetric, hairpin, horseshoe and lambda-shaped vortices. For brevity, all such vortical structures will be referred to as hairpin vortices in the remainder of this text.

Once a hairpin vortex spawns a new generation of hairpin vortices, the resultant local flow region containing multiple scales of vortical structures is commonly referred to as a turbulent spot (Emmons, 1951; Tani & Hama, 1953; Schubauer & Klebanoff, 1956; Hama et al., 1957). As a young turbulent spot convects in the streamwise direction, it grows in the lateral and longitudinal directions in considerable part by the aforementioned mechanism of generation of new wave packets.

The leading edge of a turbulent spot appears like a turbulent region overhanging a laminar region near the wall, and the length of this region may be multiples of the local boundary-layer thickness (Wygnanski et al. 1976). A calmed region where the local flow exhibits increased stability relative to the local undisturbed boundary layer is typically observed in the wake of the turbulent spot (Schubauer & Klebanoff, 1956). This calmed region suggests that the local instantaneous boundary layer deviates from the undisturbed laminar flow in a manner that increases its stability. A vortex at the trailing edge of the spot that brings high-momentum flow from the upper boundary layer toward the surface, producing a fuller and thus more stable velocity profile (Johnson, 2001). Hairpin packets at the trailing-edge of the spot produce an in-rush of high-momentum fluid from higher regions in the boundary layer to produce the calmed region (Sabatino & Smith, 2008). However, Brinkerhoff and Yaras suggest that a different mechanism may be responsible for the formation of the calmed region. The downwash motion is created by streamwise aligned layers of enhanced spanwise vorticity that extend from the spot into the wake. This motion coincides with the locations of the high-momentum streaks observed within the wake. As the spot convects downstream, the fluctuating spanwise vorticity embedded in the slower-moving fluid near the wall extends from the spot's trailing edge into the wake, inducing downwash motions and producing a calmed region that grows in sync with the longitudinal growth of the spot. In a boundary layer undergoing natural transition, multiple turbulent spots are simultaneously created at a preferred streamwise location and at predictable rates per unit time and spanwise distance. Spatial growth of these spots results in their eventual mutual merging, thereby producing a fully turbulent boundary layer.

The development of a turbulent spot in a high-disturbance environment in many ways follows a pattern similar to the one described here for natural transition. One significant variation pertains to the process of initiation of the spot. The boundary layer filters out the higher-frequency vertical disturbances in the free stream fluid, while only selected frequency disturbances to penetrate into the slower boundary layer fluid. This phenomenon is referred to as shear sheltering (Hunt & Durbin, 1999). As these free-stream disturbances penetrate the boundary layer, the fluctuations take the form of longitudinal streaks of high and low streamwise velocity near the wall in the boundary layer (Klebanoff, 1971). After the formation of streamwise streaks in the boundary layer, secondary instabilities develop and lead to formation of turbulent spots. Furthermore, the streaky structures and the resultant wavepackets in the spot tend to be less organized owing to the effects of prevailing free-stream disturbances. The manner in which the environmental disturbances modify the internal dynamics of a turbulent spot are likely dependent on the specific nature of the disturbance, which may take the form of free-stream turbulence, surface roughness, surface vibration, and other possible mechanisms (Sankaran & Antonia, 1988; Katz, Seifert & Wygnanski, 1990; D'Ovidio, Harkins & Gostelow, 2001a,b; Yaras, 2007).

CHAPTER TWO
LITERATURE REVIEW

2.1 Literature Review

Surface geometric patterns aligned with the main flow direction, so-called riblets, are well known for manipulating the stability characteristics of a laminar boundary layer and the turbulence characteristics of a turbulent boundary layer. The attractiveness of this surface modification is passiveness of the process through which these flow manipulations are realized. Riblets have a significant effect on the T-S waves and coherent structures of boundary-layer turbulence; however their impact is different for each of them. The T-S waves are amplified; whereas three-dimensional Λ-vortices may be damped by riblets (Klumpp et al., 2010). In addition, riblets may accelerate early stage of transition, while they have a tendency to reduce turbulence activity in the later stages of transition (Grek et al., 1996).

Longitudinal grooves that form between riblets may stabilize or destabilize the travelling wave instability of a laminar boundary layer, which is an inviscid instability mechanism, depending on the lateral spacing of the grooves quantified via the groove wavenumber (J. M. Floryan et al., 2015). If the groove wavenumber (β) is larger than $\beta_{tran}\approx 4.22$, the groove destabilizes the flow; for smaller values of β, the flow is stabilized. β_{tran} does not appear to depend on the groove amplitude (the depth of groove) (J. M. Floryan et al., 2014). Although this instability mode consists of travelling waves, these waves are considerably different than T-S waves in terms of their characteristics. The boundary layer becomes stable with respect to high frequency travelling waves that cause transition in the absence of the riblets (Grek et al., 1995). The riblets are able to reduce the intensity of the velocity streaks in the boundary layer. This appears to be the result of reduced magnitudes of cross-stream momentum exchange in the presence of riblets that act as a barrier to the cross-stream momentum, therefore reducing the spanwise velocity non-uniformity (Boiko et al, 2007). This observation is consistent with the reduced magnitude of near-wall velocity fluctuations in the presence of riblets as noted by Goldstein and his coworkers (Goldstein et al., 1995; Goldstein & Tuan, 1998). Weakening of the streaks, in turn, is expected to alter the stability modes associated with streaky structures reviewed in the Introduction section.

Apart from the aforementioned effects on the travelling instability mode and the structure of velocity streaks, riblets also affect the T-S instability mode, for the time-averaged profile of streamwise velocity and hence the wall-normal distribution of shear stress are modified by the riblets particularly in the near-wall region.

Most published literature on the fluid dynamics effects of surface riblets focus on the resultant changes in surface drag rather than the fundamental flow physics. First systematic studies in this context were performed by Walsh (1982) who observed skin-friction drag reduction of up to 8% with triangular or scalloped riblets with spacings less than 25 wall units and heights less than 15 wall units. Flow structures and turbulence statistics strongly depend on riblet spacing. The spanwise spacing of the riblets in relation to the hairpin vortices residing close to the surface dictates whether the riblets cause a net increase or net decrease in surface skin friction drag (Suzuki & Kasagi, 1994). Riblets are generally categorized as either closely-spaced (15-25 wall units) or widely spaced. For closely-spaced riblets, the spacing corresponds to 30 to 50% spanwise extent of the streamwise leg of the hairpin vortices. This spacing enables the riblets to interfere with the development of cross-flow motion (Goldstein et al., 1995, Goldstein & Tuan, 1998). It has been hypothesized that the inhibition of the spanwise motions of the low-speed fluid in the riblet-wall region results in a decrease in the effectiveness of the ejection events (Chu & Karniadakis, 1992). Further, the streamwise-oriented legs of the hairpin vortices are observed to move away from the surface, residing in the vicinity of the riblet tips (Choi et al., 1993; Lee & Lee, 2001). Both effects promote lower wall shear stress, thereby reducing the skin friction drag (Djenidi & Antonia, 1993; Goldstein et al. 1995; Bechert et al., 1997). The closely-riblet surface produces weaker hairpin vortices due to weaker upwash motions (Klummp et al., 2010). The shear layer with weakened streaks does not develop the secondary instabilities and tend to produce fewer hairpin vortices (Chernorai et al., 2006; Boiko, 2007). When the riblet spacing is more widely, they are less effective in the damping spanwise fluctuations, hence the cross-flow can penetrate into the grooves and then wash over the next riblet (Goldstein & Tuan, 1998).

The foregoing literature review discussed above shows that the topics like the shape, height, and spacing of the riblets and their effects on the drag reduction have been widely investigated. In this thesis, it is aimed to understand how the riblets modify the coherent flow structures within a turbulent boundary layer and to investigate the changes in the development cycles of hairpin vortices induced by the presence of riblets through direct numerical simulation.

CHAPTER THREE
COMPUTATIONAL SETUP

3.1 Computational Domain

The simulation is performed based on a spatial domain shown in Figure 3.1, which consists of riblets aligned in the streamwise direction. All dimensions in this figure are shown normalized by δ_0^*, which has as a value of 1.44 mm and corresponds to the displacement thickness of the undisturbed boundary layer for the smooth surface at the streamwise location of the jet orifice. The orifice is used to inject a jet into the mainstream for a brief period to create a disturbance that is strong enough to produce a turbulent spot. A free-slip surface is placed upstream of the no-slip test surface to allow the boundary layer to develop naturally starting at the leading edge. A free-slip surface placed immediately downstream of the no-slip surface ensures natural development of the boundary layer up to the trailing edge of the no-slip surface without any artificial influence by the boundary condition imposed on the outflow boundary. Based on the results of previous simulations, the domain width is sized such that the free-slip side boundaries are more than $30\delta_0^*$ away from the closest edge of the turbulent spot at its most mature stage in the domain. The domain height is chosen such that the domain free-slip ceiling is sufficiently far from the no-slip surface such that the presence of the ceiling does not artificially influence the development of the boundary layer and the flow structures within the turbulent spot, which grow to a maximum height of not more than $15\delta_0^*$. The domain height at the outflow end is set to be slightly larger than that at the inflow end to offset no-slip test surface due to the riblets, which are placed starting at $125\delta_0^*$ from the test surface leading edge. A spatially-uniform velocity with a magnitude of 4.55 m/s and aligned in the x direction is specified at the inflow boundary of the domain. Static pressure that is kept fixed in an area-averaged sense at a gauge value of 0 Pa is specified at the outflow boundary of the domain. A turbulent spot is generated in the domain by ejection of working fluid perpendicular to the test surface through a rectangular orifice for a duration of t_{jet}. The dimensions of the subdomain representing the rectangular pipe feeding this orifice are shown in an inset in Figure 3.1. The spatially-uniform velocity at the inflow boundary of this subdomain is set to 35 m/s for a duration of t_{jet} = 8.54 ms, and the no-slip condition is imposed on its four walls.

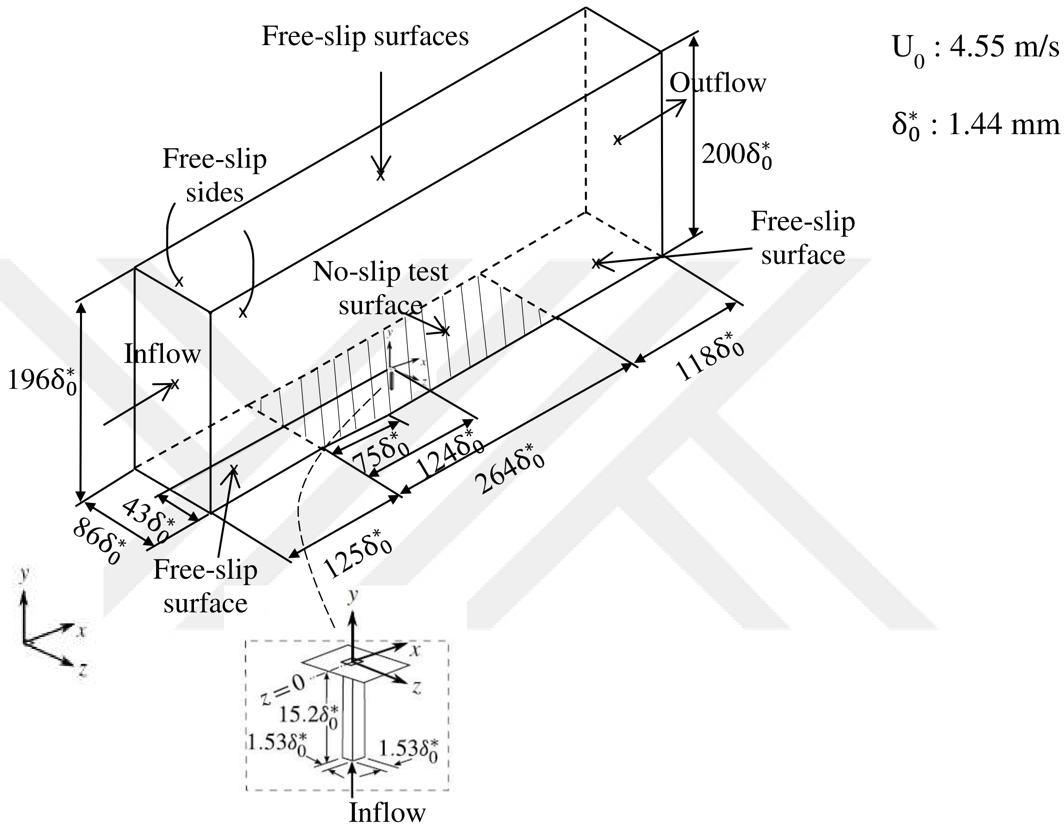

Figure 3.1 Schematic of the computational domain

3.2 Test Surfaces

The present study examines the development of a turbulent spot over a surface with streamwise riblets and compares this development to that on a smooth surface. The spanwise spacing of low-speed streaks is approximately 100 wall units based on average wall shear stress within the turbulent spot under zero streamwise pressure gradient (Gad-El-Hak et al., 1981). However, when the pressure gradient is strongly favourable, spanwise spacing of low-speed streaks are two or three times larger than zero pressure gradient boundary layer (Yaras, 2007). The present computational domain and its boundary conditions were set to achieve nominally zero streamwise pressure gradient. Accordingly, the riblets were spaced at 100 wall units, matching the spacing of the velocity streaks observed on smooth surfaces. This choice was not based on the expectation that it would be optimum for achieving the most effective manipulation of the turbulence prevailing in the turbulent spot. Rather, the present configuration is deemed as the first step in understanding the manner in which the spot turbulence is modified by the presence of riblets, which would then inform future studies with optimized riblet spacings. The height of the riblets is set to 75 wall units, which concentrates the effects of the riblets to the near-wall region where the streamwise legs of the hairpin vortices reside. The viscous length scale, u_τ/ν, is calculated based on the average wall shear stress over the footprint of the turbulent spot at its most mature state as it develops along the length of the test surface over the smooth surface. This wall shear stress is estimated based on the correlations for fully turbulent boundary layers proposed by Schlichting (1968). This approach is justified on the basis of favourable agreement noted by Brinkerhoff & Yaras (2014) between the predictions with these correlations and the results of direct numerical simulations of turbulent spot. The cross-sectional view of the riblets and related dimensions are shown in Figure 3.2. The trapezoidal riblet geometry was chosen instead of triangular or rectangular alternatives to produce wider-angled corners, thus promoting streamwise flow within the grooves formed by the riblets, and to avoid sharp tips that may be more prone to damage in practical applications. The riblets start with zero height at $125\delta_0^*$ from the test surface leading edge, and grow linearly in height until they reach their terminal height at $200\delta_0^*$ from the leading edge.

The results of the simulation with the riblet surface are compared to those for a smooth surface. The smooth-surface simulations were performed by Brinkerhoff and Yaras (2014).

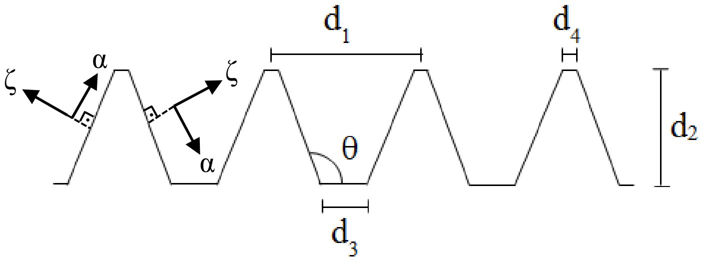

Dimension	Value
d_1	7.5 mm
d_2	5.56 mm
d_3	2.38 mm
d_4	0.4 mm
θ	133.2°

Figure 3.2 Riblet geometry and dimensions

3.3 Base flow and turbulent spot initialization

The simulation is initialized with a uniform velocity value of U_0 = 4.55 m/s in order to develop a laminar boundary layer on the riblet surface and is marched in time until convergence to steady state. Subsequently, a flow perturbation is created via the jet ejected through the orifice on the test surface. The magnitude of the velocity of the jet is set to $7.7U_0$. This jet is activated for a duration of τ_{jet} = 27 time units, where $\tau = tU_0/\delta_0^*$ is the dimensionless time coordinate. The instant when the jet is turned off corresponds to $\tau = 0$ and simulation is continued until $\tau = 303$.

3.4 Spatial and Temporal Grids

The spatial grid consists of a structured grid formed by hexahedral cells. The number of nodes in the streamwise (x), spanwise (z), and wall-normal (y) directions in the computational domain and the cross-sectional view of the grid are shown in Table 3.1 and Figure 3.3, respectively. The grid-node distribution is optimized to ensure resolution of all relevant flow features. The smallest-scale turbulence structures in the turbulent spot dictate the level of grid refinement in close vicinity of the no-slip surface. This, together with the need to limit the rate of change of the grid-node spacing in the three coordinate directions to less than 10%, determines the node distribution throughout the computational domain. The 10% limit is imposed based on the experience of the authors' research group with this algorithm for achieving accurate simulation results.

Table 3.1 Number of nodes in the spatial grid

	N_x	N_y	N_z
Domain	391	88	398
Jet subdomain	60	88	60

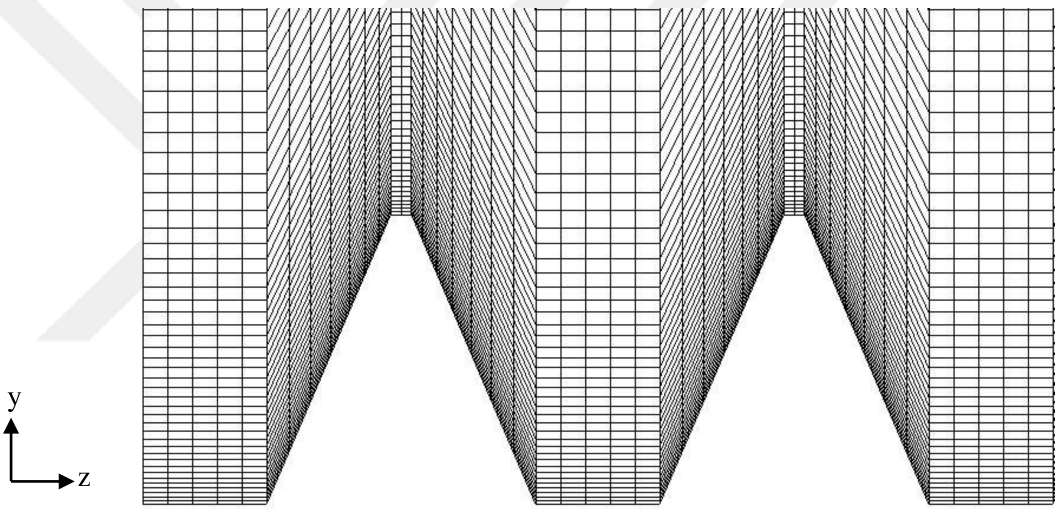

Figure 3.3 Cross-sectional view of the grid in the vicinity of the two riblets

The smallest scale of turbulence in a turbulent boundary layer is on the order of the Kolmogorov length and time scales. The Kolmogorov length scale has a value of $\eta^+ \approx 2$ at locations close to a wall boundary (Kim et al., 1971; Pope, 2000; Stanislas et al., 2008), where η is the Kolmogorov length scale and + superscript denotes normalization by the viscous length scale, u_τ/ν. Here, $u_\tau = \sqrt{\tau_w/\rho}$ is the friction velocity, τ_w is the wall shear stress, ν is the kinematic viscosity and ρ is the density of the working fluid.

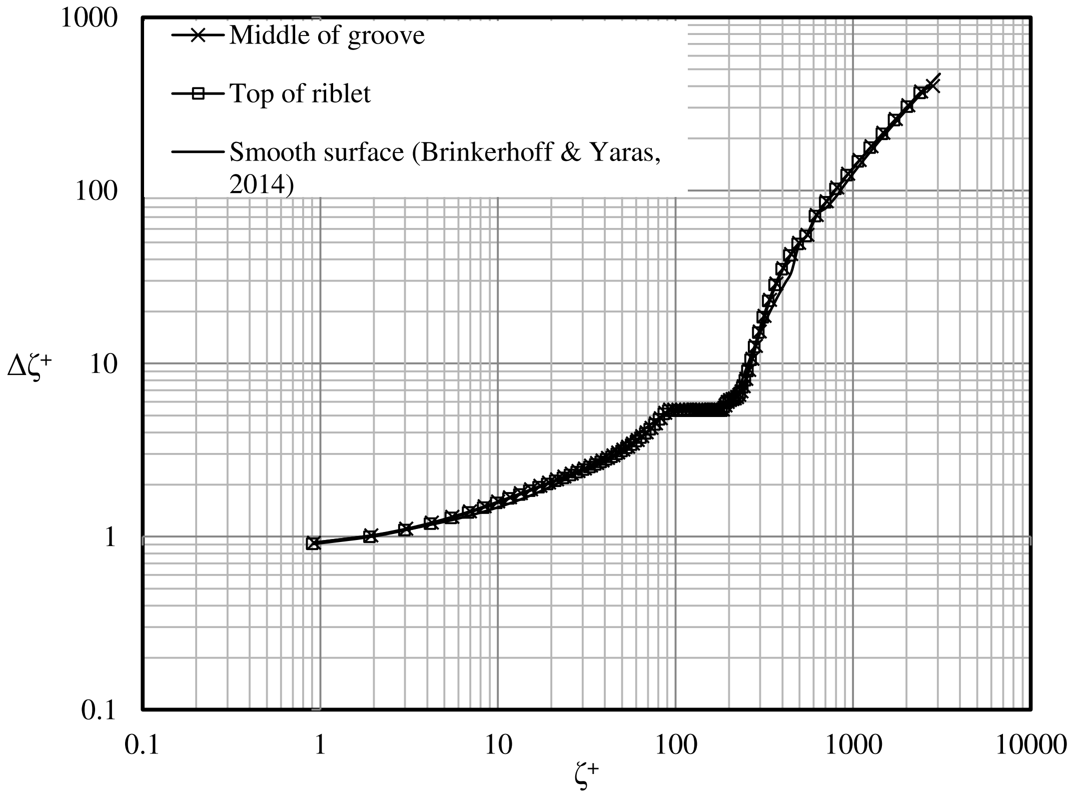

Figure 3.4 Wall-normal node distribution

The wall-normal positioning of the grid nodes is described via the α - ζ coordinate as defined in Figure 3.3. The first node adjacent to the wall surface is placed at $\zeta^+ \leq 0.9$. From this first node to a wall-normal distance of $\zeta^+ = 30$, the node spacing is increased linearly such that 18 nodes are placed within this range of wall-normal distance. Beyond this range, the node spacing is increased at a rate of 4% up to $y/\delta_0^* = 5.0$, held constant up to $y/\delta_0^* = 8.7$ and then increased at a rate of 10% until the free-slip ceiling of the domain is reached. This node distribution is shown in Figure 3.4.

The streamwise and spanwise node distributions are shown in Figure 3.5 and Figure 3.6, respectively. In the streamwise direction, the first node adjacent to the inflow boundary surface is placed at the x^+ value of 34.6. From this first node to a streamwise distance of $x^+ = 2460$, the node spacing is decreased at a rate of 5% such that 175 nodes are placed within this range of streamwise distance. Beyond this range, the node spacing remains constant around the jet subdomain, and then increased linearly at a rate of 10% until the outlet of the domain is reached. This streamwise node distribution is same as that used for the smooth surface simulation by Brinkerhoff & Yaras (2014).

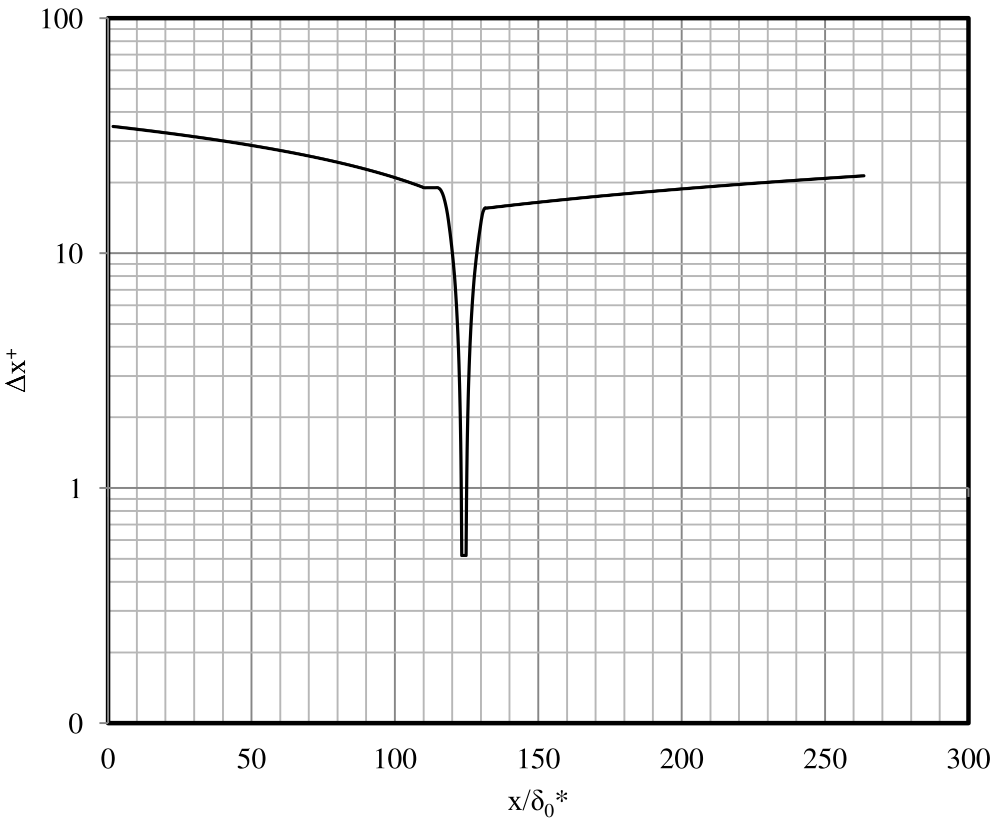

Figure 3.5 Streamwise node distribution

In the spanwise direction, α^+ value of 6.6 is used within the groove centers, except the groove corresponding to the jet subdomain. This base of the groove is discretized with 60 nodes in the spanwise direction. At the side walls of riblets, the node spacing is decreased and increased at a rate of 5% from the base of the groove to the riblet tip and from the riblet tip to the base of the groove resulting in 7 nodes along each side wall of the riblet.

In comparison, the spanwise node distribution in the smooth-surface simulation of Brinkerhoff and Yaras involved clustering of the nodes towards the location of the jet orifice, with a Δz^+ value of 0.5 at the jet orifice, a Δz^+ value of 8.4 at the side walls of the computational domain, and a rate of change of node spacing in the spanwise direction that remained less than 10%.

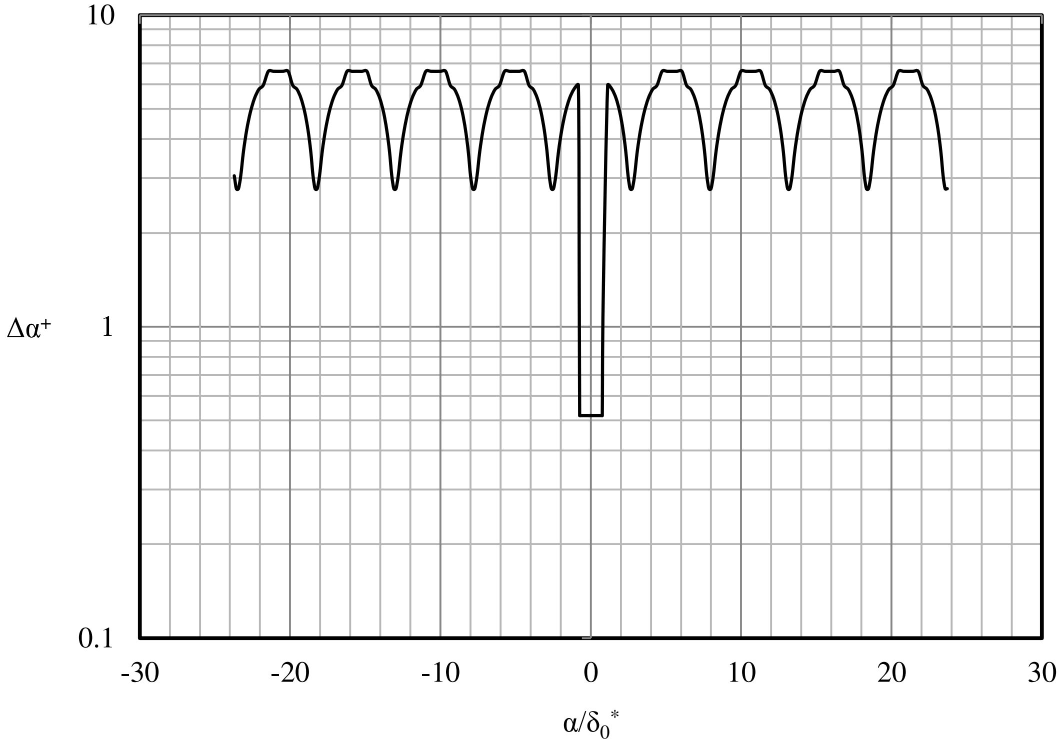

Figure 3.6 Spanwise node distribution

The jet subdomain is discretized with 60 nodes in the x and z directions. The direction parallel to the jet flow (y) is discretized with 88 nodes that are distributed such that of these 15 nodes are placed within $1\delta_0^*$ distance of the jet discharge plane. The node spacing at the jet discharge plane is $\Delta y^+ = 0.65$ and the spacing increases in the -y direction at a rate of less than 10% until $\Delta y^+ = 4.0$, beyond which the node spacing remains constant up to the inflow plane of the jet subdomain.

Timestep size of $\Delta t = 7 \times 10^{-6}$ s is chosen for the simulation. This value corresponds to a maximum normalized timestep of $\Delta t^+ = 0.11$, where $t^+ = {}^{\nu}/_{u_\tau^2}$ is the viscous time scale for the most mature state of the turbulent spot on the smooth surface. This normalized value is smaller than the timestep size of $\Delta t^+ = 0.2$

recommended by Choi & Moin (1994) for accurately capturing the temporal growth of turbulence structures.

3.5 Solution method

The commercial software package ANSYS CFX is used to solve the mass and momentum equations discretized using the finite-volume approach. The spatial interpolations used in the integration-based finite-volume approach correspond to second-order central differencing and second-order Euler backward differencing for discretization of the spatial and temporal derivatives, respectively. Convergence is declared when the root mean square (rms) value of the normalized residuals of these equations are reduced to $1x10^{-6}$, which was established to be a sufficiently low threshold to achieve accurate results by Brinkerhoff and Yaras, 2014. This threshold was established based on a validation simulation described in the next section. Iterative solution of the mass and momentum equations within each time step involves W-type multigrid cycles with six grid levels. One solution sweep is performed on each grid level during the restriction leg of the cycle, and three solution sweeps are performed during the prolongation phase. A single multigrid cycle (inner iteration) is performed for a given set of frozen coefficients of the linearized equations, and the coefficients are updated up to eight times (outer iterations) within each time step to achieve the above-noted residual levels.

3.6 Validation of the Numerical Approach

The suitability of the numerical algorithm and spatial and temporal grids is validated by the author's research group via a series of direct numerical simulations of zero-pressure-gradient turbulent boundary layer. The results of these simulations were compared to published experimental and computational statistical turbulent properties of corresponding turbulent boundary layers.

The validation simulation was run at a Reynolds number based on the boundary layer momentum thickness of $Re_\theta = 900$ and a spatial resolution in the streamwise-spanwise plane of $\Delta x^+ = 3$ and $\Delta z^+ = 3$. In the present study, greater Δx^+ values are used upstream of the jet orifice, but downstream of this location, a finer grid is used to capture the turbulent coherent structures, such that a spatial resolution in the streamwise direction of $\Delta x^+ = 1.4$ is used in the streamwise region where the turbulent spot develops on simulation. In the spanwise direction, spatial resolution of the present simulation is similar to that of the close with validation simulation. The y^+ value of the first node from the no-slip boundary is 0.85 and over a wall-normal distance of $y^+ = 30$, the node spacing is increased linearly such that 18 nodes are placed within this range of wall-normal distance. Beyond this range, the node spacing is increased at a rate of 4% up to $y/\delta_0^* = 5.0$, held constant up to $y/\delta_0^* = 8.7$ and then increased at a rate of 10% until the free-slip ceiling of the domain is reached. The rates of turbulence kinetic energy production (P^+) and dissipation (ε^+) and the mean velocity profile (U^+) at the target Reynolds number are shown in Figure 3.7. The results were compared to the studies by Mansour et al. (1988) who used the simulation data of a turbulent channel flow of Kim et al. (1987) at $Re_\tau = 180$ based on the channel half-height and the mean friction velocity to compute the terms in the transport equations for the Reynolds stresses and to compute the terms in the transport equation for the dissipation rate of turbulence kinetic energy and to the experimental results of Klewicki et al. (1990). The simulation data used in the study of Mansour et al. (1988) were obtained by solving the governing equations using a spectral method based on Fourier series in the streamwise and spanwise directions, Chebychev polynomial expansions in the wall-normal direction and besides second-order Crank-Nicolson scheme for temporal discretization. Figure 3.7 shows that the rates of turbulence production and dissipation and the mean velocity profile of these validation simulations compare well with published results.

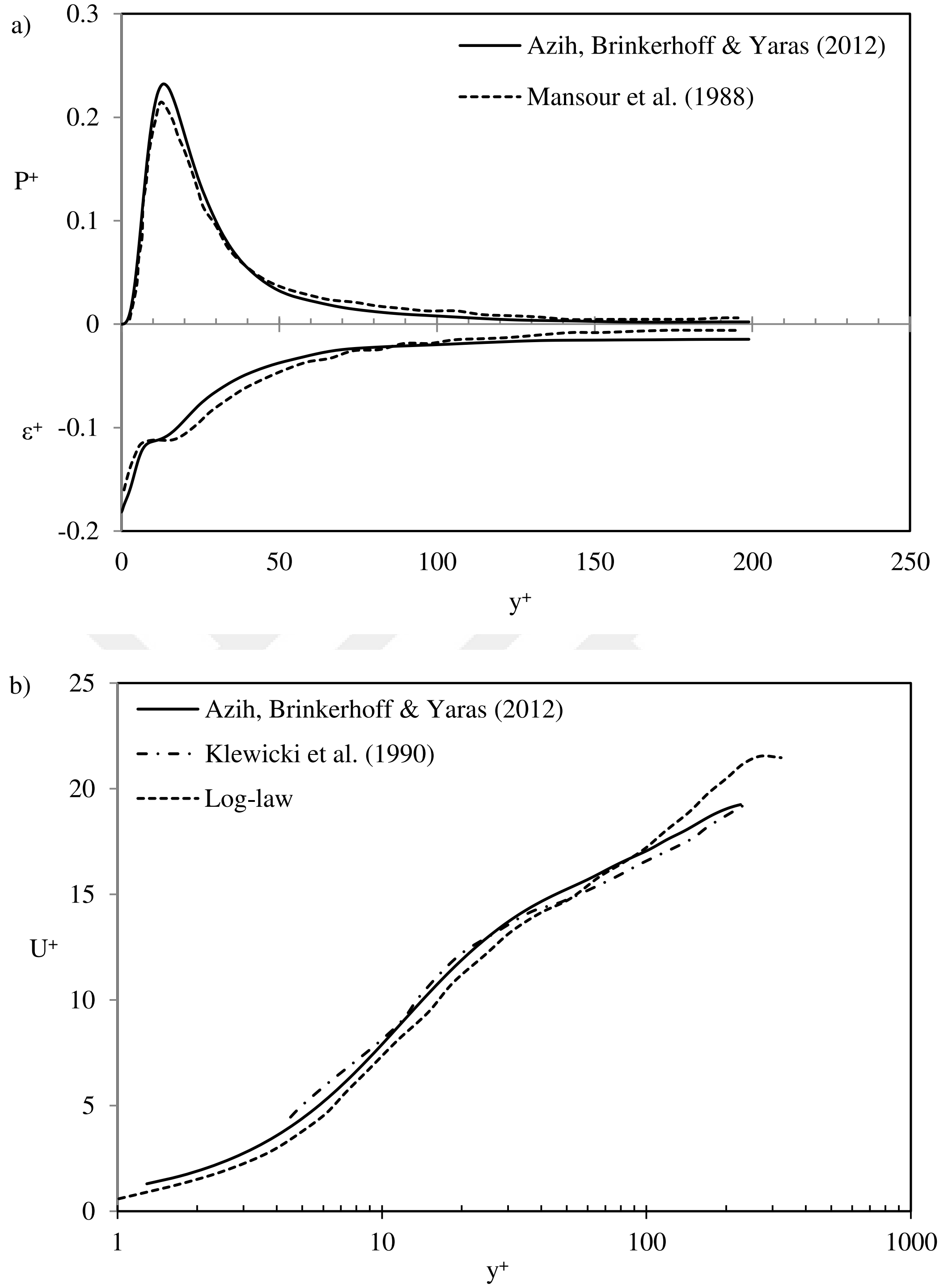

Figure 3.7 Validation DNS study of a zero-pressure-gradient turbulent boundary layer (Re_θ = 900, Re_τ = 250). Compared with (a) turbulence kinetic energy production (P^+) and dissipation (ε^+) rates of Mansour et al. (Re_τ = 180), and (b) the mean velocity profile of Klewicki et al. (Re_θ = 1010)

CHAPTER FOUR
RESULT AND DISCUSSION

4.1 Laminar Baseflow

The streamwise distributions of the freestream velocity, U_e, and the streamwise acceleration parameter, $K = \nu/U_e^2\ dU_e/dx$, are presented in Figure 4.1. $x_{jet}/\delta_0^* = 0$ indicates the jet location. The free-stream acceleration parameter is close to zero along the test surface as intended, yielding a zero-pressure-gradient undisturbed boundary layer prevails over the test surfaces.

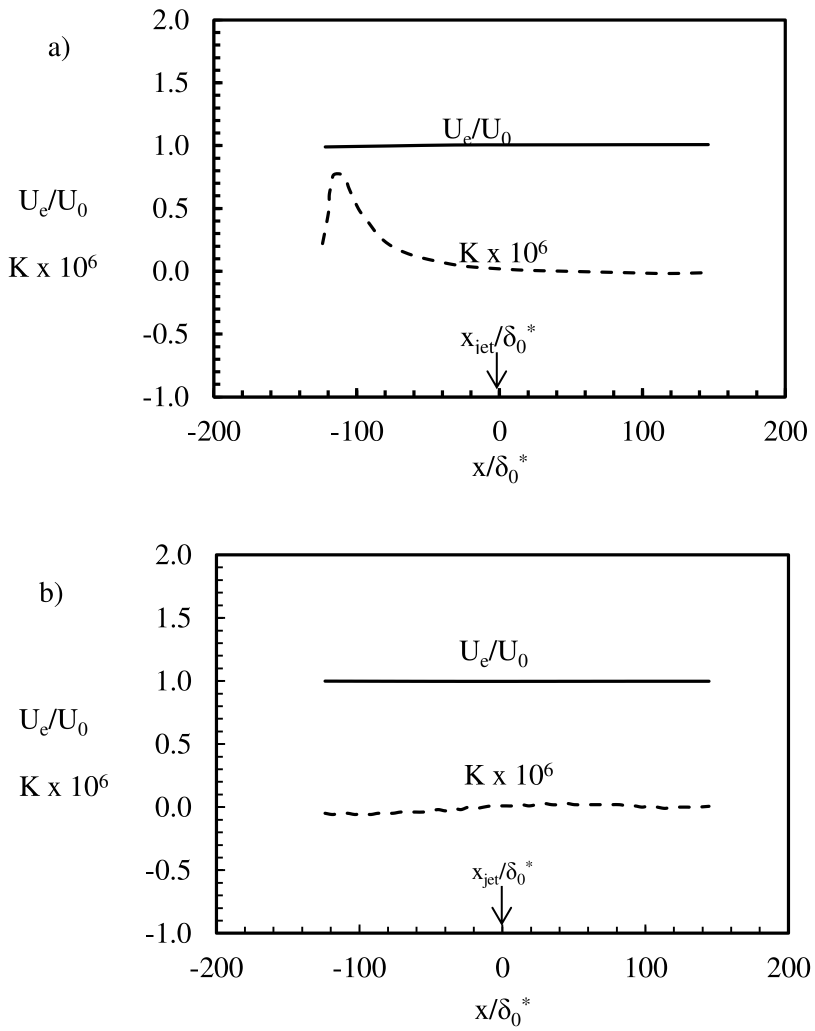

Figure 4.1 Streamwise distributions of the free-stream velocity, U_e, and streamwise acceleration parameter, K, on a) smooth surface and on b) riblet surface

Figure 4.2 illustrates the laminar, undisturbed streamwise velocity profiles at the riblet centerline, at the groove centerline and on the smooth surface. The boundary layer on the riblet tip appears to develop in a manner very similar to that on the smooth surface. In the groove, however, the combined flow retarding effect of the side walls and the groove base results in greater momentum deficit. For reference, the riblet height corresponds to $3.86\delta_0^*$. Accordingly over the test-surface length considered, the boundary layer developing on the base of the groove is mostly confined to the groove. As such, not surprisingly, the above-noted drag effect of the groove walls affects the boundary layer across its full thickness.

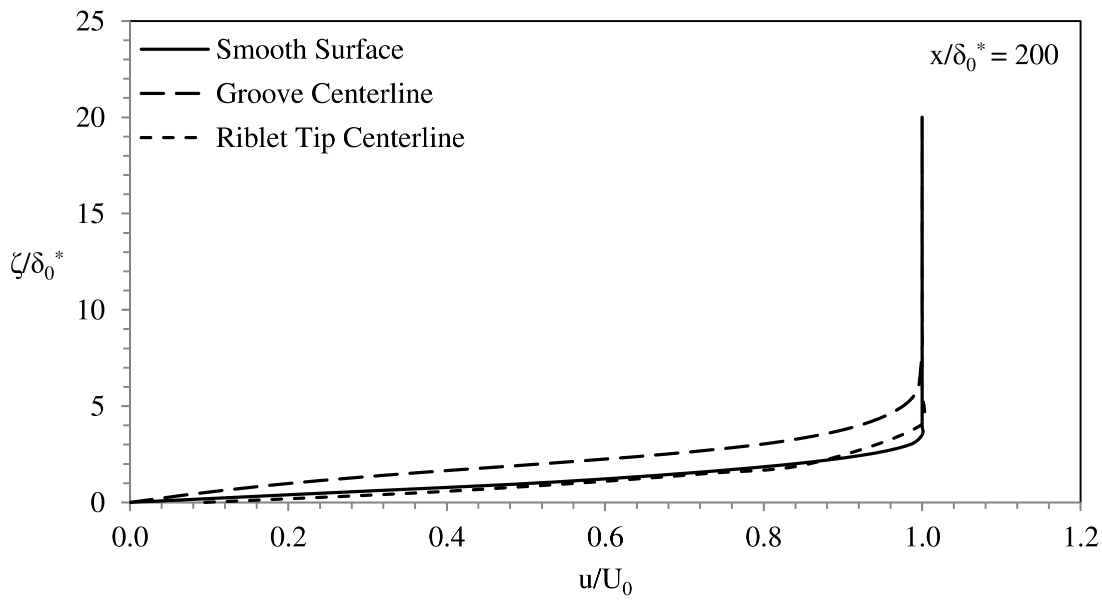

Figure 4.2 Undisturbed boundary layer velocity profiles at $x/\delta_0^* = 200$

The comparison of the boundary layer development on the riblet tip, the groove and the smooth surface as presented in Figure 4.2 is limited to the centerline of the riblet tip and the centerline of the groove. In the groove, the mass deficit is expected to be higher near the side walls than at the centerline. Comparison of the mass flow rates and their streamwise variations in strategically defined flow zones may help to provide insight into the extent of mass flow redistribution prompted by the presence of the riblets. These zones are defined in Figure 4.3a for the riblet surface, and are complemented by corresponding zones on the smooth surface shown in Fig. 4.3b. The height of Zone 2 on the riblet surface is set such that this zone extends well beyond the boundary layer at all streamwise locations. The height of Zone 3 on the smooth surface is set to match that of Zone 1, and the width of Zone 3 is set such that the mass flow rate in this zone at $x/\delta_0^* = -120$ is the same as that in Zone 1 at the same streamwise location. Likewise, the height of Zone 4 on the smooth surface is set to match that of Zone 2, and its width is set such that Zone 2 and Zone 4 have the same mass flow rate at $x/\delta_0^* = -120$. Streamwise variations of mass flow rate in all four zones, normalized by the corresponding mass flow rates at $x/\delta_0^* = -120$ are shown in Figure 4.4.

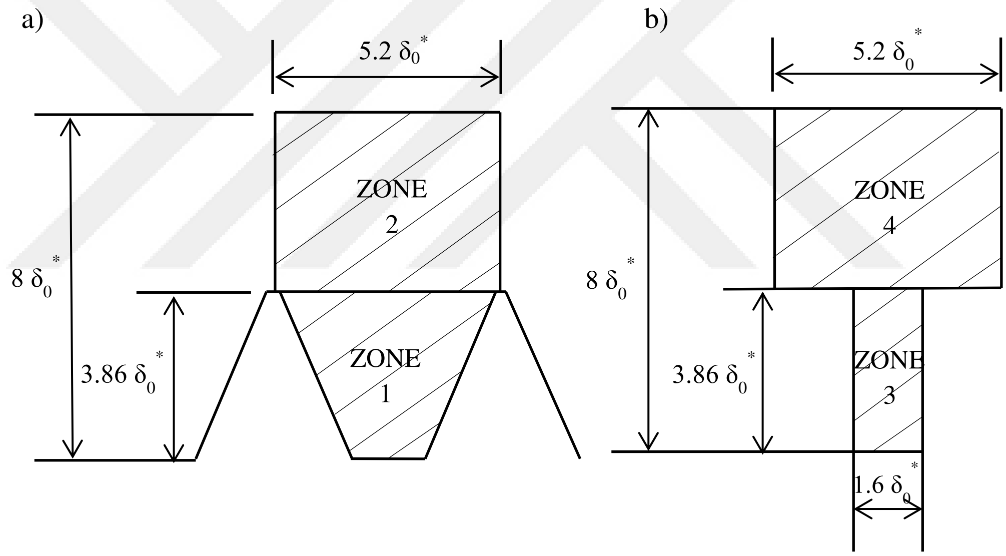

Figure 4.3 Mass flow integration zones a) riblet surface, b) smooth surface

Because of the ramp which located at the beginning of the test surface, the height of the riblets increase linearly until their terminated value. After the end of ramp, the height of the riblets is constant. In the light of this geometric information, it is observable that the mass flow rate within the Zone 1 has a rapid decline along the riblet test surface compared to the Zone 3, as shown in Figure 4.4. Although, Zone 1 has greater area than Zone 3, the velocities within the Zone 1 are pretty low compared to the velocities within the Zone 3, because of the no-slip riblet side walls. The flow is faced with greater viscous forces in the groove in Zone 1 compared to the smooth surface in Zone 3. It is clear that the low-momentum fluid is observable within the riblet grooves.

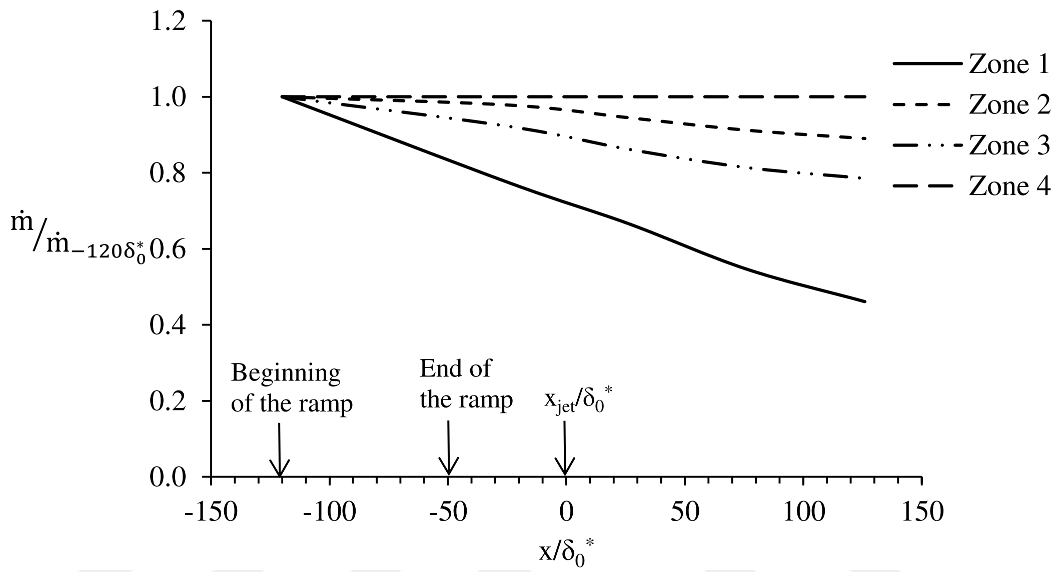

Figure 4.4 Mass flow rate at different streamwise directions

A slightly decrease is observed on mass flow rate depends on the development of laminar boundary layer over the smooth surface in the Zone 3. In the Zone 4, the streamwise velocity is the constant freestream velocity, because the Zone 4 is located above the laminar boundary layer. The mass flow rate is not change in the Zone 4 that has a constant area during the test surface. Although the Zones 2 and 4 are the same width and height and located the same wall-normal and spanwise coordinates, the velocities change depends on the streamwise distance, so Zone 2 is not completely out of the laminar boundary layer. These results shows that the riblet surface induces to raise the laminar boundary layer over the riblet surface higher levels compared to the smooth surface.

4.2 Turbulent Spot Development

The jet leads to the growth of the coherent flow structures within the turbulent spot, creating the vortices in the boundary layer (Fric & Roshko, 1994). When the main-flow boundary layer convects around the jet and an adverse pressure gradient is created behind the jet, it separates and vertically-oriented vortices roll up in the jet flow near the corners of the jet orifice immediately above the orifice. These vortices are the 'seed' that initiates the formation of the turbulent spot (Brinkerhoff & Yaras, 2012).

Vertically-oriented vortices roll up immediately in the jet flow near the corners of the jet orifice. Spanwise-oriented vorticity originating in the jet channel boundary layer along the downstream jet channel wall is re-oriented in the streamwise direction by the velocity field induced by the corner vortices (Brinkerhoff and Yaras, 2012). These counter-rotating streamwise-oriented vortices grow in the streamwise direction downstream of the orifice over the duration of the jet pulse. They lift the spanwise vorticity in the main-flow boundary layer away from the wall immediately downstream of the jet resulting in the formation of one hairpin-shaped vortex straddling each streamwise-oriented vortex. The legs of these hairpin vortices extend to the wall on either side of the corresponding streamwise vortex (Brinkerhoff and Yaras, 2014).

Figure 4.5 illustrates that the vertical structures which are visualized using iso-surfaces of the second invariant of the velocity gradient tensor normalized by $(U_0/\delta_0^*)^2$, denoted Q, defined as:

$$Q = \frac{1}{2}\left(\frac{\partial u_i^2}{\partial x_j} - \frac{\partial u_i}{\partial x_j}\frac{\partial u_j}{\partial x_i}\right)$$

where u_i and u_j represent the components of the perturbation velocity vector and Einstein summation is implied over the indexed terms. Perturbation quantities in the present study are defined as the difference between the instantaneous and undisturbed flow fields. The value of Q at which the iso-surfaces are plotted is chosen to most clearly show all vortical structures which affect the dynamics of the flow. The iso-contours are coloured according to the value of y/δ_0^* to aid in comparing the relative heights of the vortical structures. At $\tau = 2$, the streamwise-oriented vortices created by the jet.

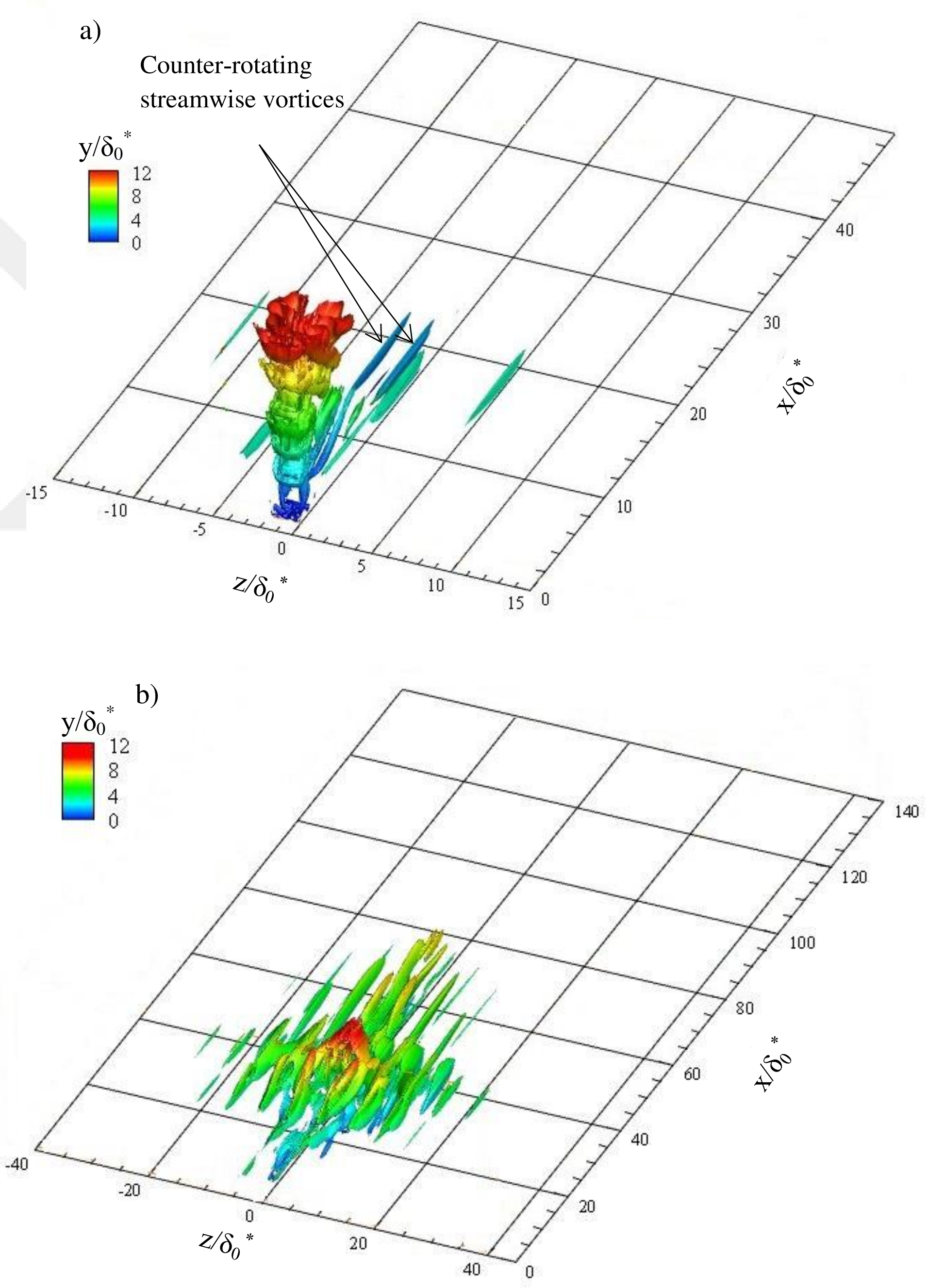

c)

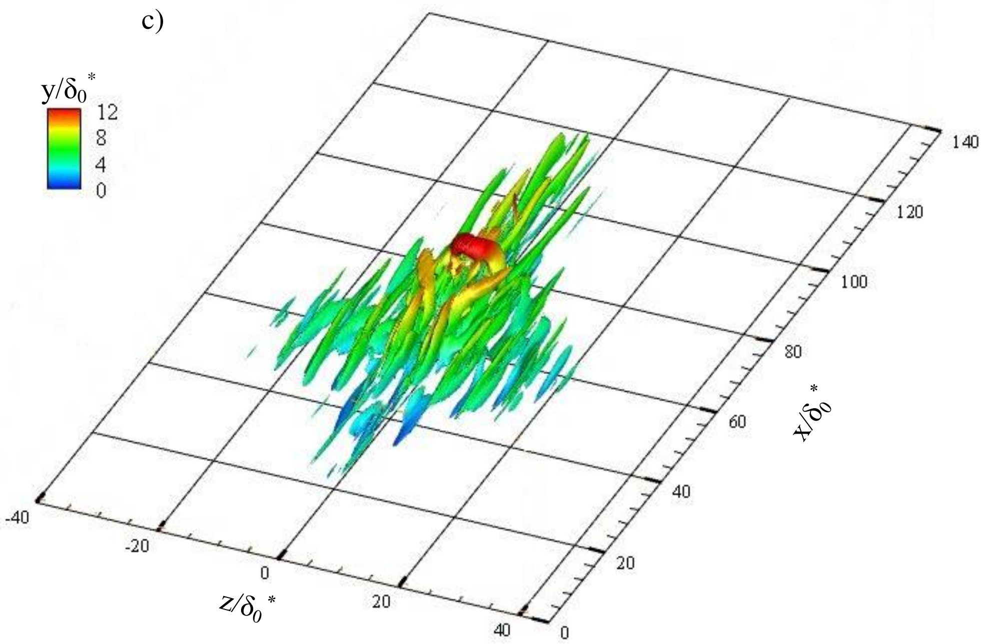

Figure 4.5 Formation of the turbulent spot illustrated at a) τ = 2, b) τ = 46 and c) τ = 90, visualized through iso-contours of Q = 0.1

The counter-rotating streamwise-oriented vortices grow in the streamwise direction downstream of the orifice over the duration of the jet pulse. They induce downwash in the region between the vortices and upwash in the region outboard of the vortices. These wall-normal motions convect the local boundary-layer vorticity closer to and farther away from the wall, respectively. These counter-rotating streamwise-oriented vortices grow in the streamwise direction downstream of the orifice over the duration of the jet pulse. They lift the spanwise vorticity in the main-flow boundary layer away from the wall immediately downstream of the jet resulting in the formation of one hairpin-shaped vortex straddling each streamwise-oriented vortex. The legs of these hairpin vortices extend to the wall on either side of the corresponding streamwise vortex. The two initial hairpin vortices grow in size as they convect downstream, eventually merging to form one larger hairpin vortex, which is the primary hairpin vortex of the turbulent spot identified. This is followed by the development of several secondary hairpin vortices upstream of the primary hairpin vortex. The smaller secondary hairpin vortices merge together into larger hairpin vortices. This is followed by the formation of tertiary hairpin vortices upstream and downstream of these secondary hairpin vortices, such that the spot is soon densely populated with coherent structures of turbulence.

4.3 Growth of the turbulent spot

The generation of new hairpin vortices upstream of existing hairpin vortices in this manner leads to groups of two or three closely spaced hairpin vortices called wavepackets, in which hairpin vortices are arranged in streamwise succession and travel downstream together at about the same speed. As wavepackets convect downstream, the hairpin vortices within them extend in the wall-normal direction due to self-induced motions and stretch in the streamwise direction due to the background wall-normal profile of streamwise velocity. Older wavepackets which are larger in size are exposed to flow with higher streamwise velocity farther from the wall, and therefore travel downstream faster than newer, smaller wave packets. This leads older, larger wave packets to overtake and mutually interact with newer, smaller wavepackets (Adrian et al., 2000). Additionally, the low population of hairpin vortices observed upstream of the trailing edge of the spot implies the development of a ‘calmed’ region in the wake of the spot; the development of this calmed region.

The upwash motion ejects the low-momentum fluid and leads to the development of the low-speed streak between the legs of the parent hairpin vortex. At the same time, the downwash motion brings the high-momentum fluid into the boundary layer on the outboard side of the parent hairpin vortex. Due to the fact that the hairpin vortex is located at the laminar/turbulent interface, the background spanwise vorticity into the streamwise direction is stretched by the downwash of high-momentum fluid on the outboard side of hairpin vortex. An inflectional streamwise velocity profile develops at the interface between the low-speed streaks and the surrounding higher-speed flow. Streamwise grouping of vorticity within this shear layer by the K-H instability mechanism leads to the roll-up of this shear layer into new hairpin vortices

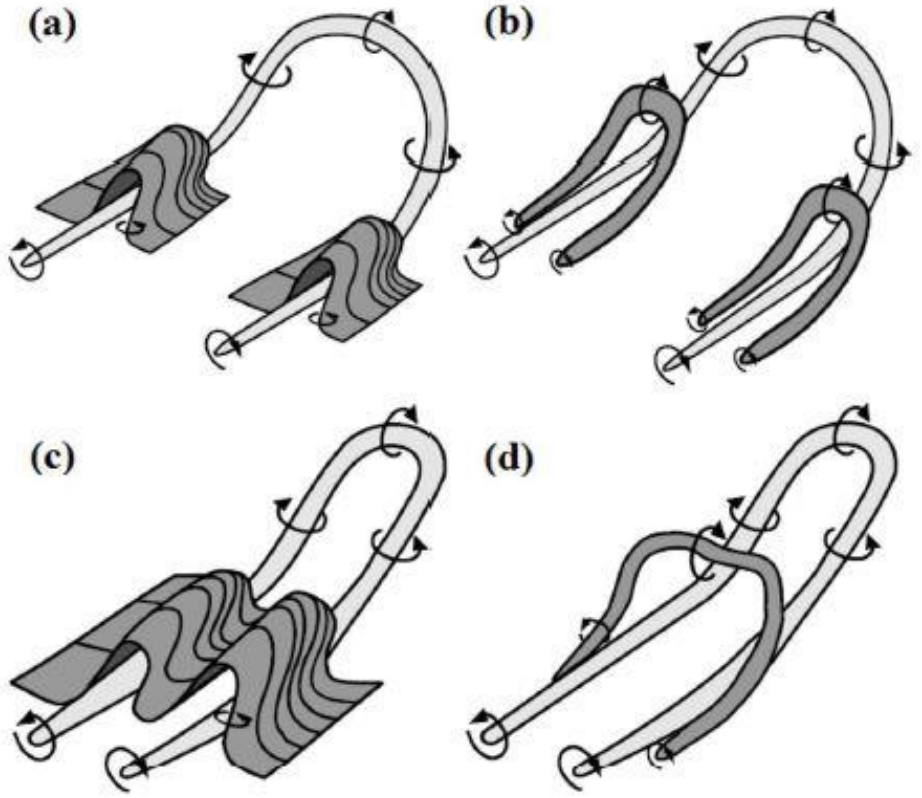

Figure 4.6 Schematic of the development of new hairpin vortices from a parent hairpin vortex with (a)-(b) widely-spaced legs and (c)-(d) closely-spaced legs; (Adapted from Brinkerhoff & Yaras, 2014)

Schröder and Kompenhans (2004) and Schröder et al. (2008) observed new hairpin vortices which straddle the nearest leg of the parent hairpin vortex, while Smith et al. (1991) and Singer and Joslin (1994) suggest that new hairpin vortices develop between the legs of a parent hairpin vortex. Both of these regeneration mechanisms of hairpin vortices can be observed in a turbulent spot (Brinkerhoff & Yaras, 2014). When the legs of the parent hairpin vortex are widely-spaced, a low-speed streak develops next to each leg. The shear layer enveloping each low-speed streak rolls up into a separate hairpin vortex, as shown in Figure 4.6a and b (Brinkerhoff & Yaras, 2014). On the other hand, when the legs of the parent hairpin vortex are closely-spaced, the regions of low-speed flow that are lifted away from the wall next to each leg merge together to form a single region of low-speed fluid. The shear layer enveloping this region evolves into a single hairpin vortex, as shown in Figure 4.6c and d (Brinkerhoff & Yaras, 2014). The first mechanism is typically observed among the large- scale hairpin vortices near the leading edge and spanwise edges of the spot, and the second mechanism is typically observed among smaller-scale hairpin vortices near the trailing edge of the spot (Brinkerhoff & Yaras, 2014).

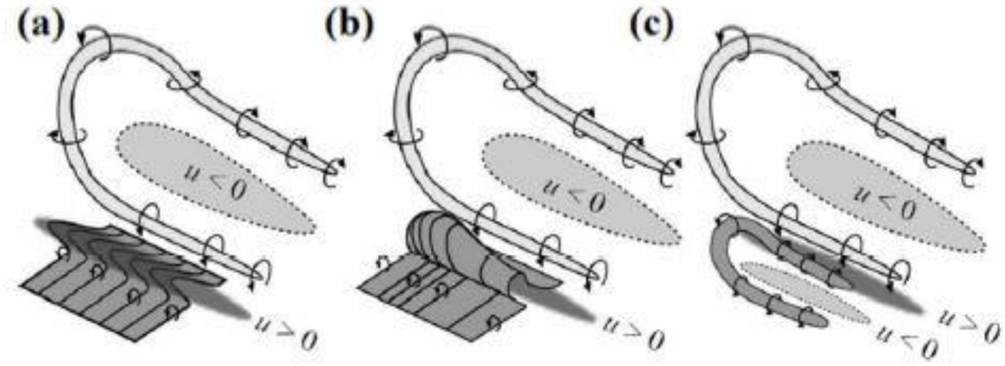

Figure 4.7 Schematic of the regeneration mechanism of wavepackets along the spot spanwise edges; (Adapted from Brinkerhoff and Yaras, 2014)

Lateral growth of the spot occurs through generation of new wave packets along the spot spanwise edges is illustrated schematically in Figure 4.7. In Figure 4.7, u denotes the streamwise component of perturbation velocity. Downwash motions on the outboard sides of the legs of hairpin vortices which reside along the spanwise edges of the spot perturb the laminar flow beyond the laminar/turbulent interface on the sides of the spot (Brinkerhoff & Yaras, 2014). The high-speed flow which is swept toward the wall stretches the background spanwise vorticity in the streamwise direction creating streamwise-oriented vorticity which lifts itself away from the wall by self-induced motions (Brinkerhoff & Yaras, 2014). The resulting shear layer rolls up into new hairpin vortices, which induce wall-normal motions to form new high and low-speed streaks along the spot spanwise edges.

4.4 Effect of Riblets on the Coherent Structures of Turbulent

Over the riblet surfaces, the turbulent spot is formed by the same bypass mechanism under freestream conditions identical to those described for the smooth surface. Any changes in the formation of the spot or the hairpin vortices within it may therefore be attributed to the difference in the near-wall flow-field created by the topology of the riblet surface. The spanwise vorticity of the undisturbed boundary layer is the primary source of vorticity for the hairpin vortices of the turbulent spot. Accordingly, the development of the hairpin vortices and their spatial organization tend to affect from the spatial distribution of vorticity in the boundary layer.

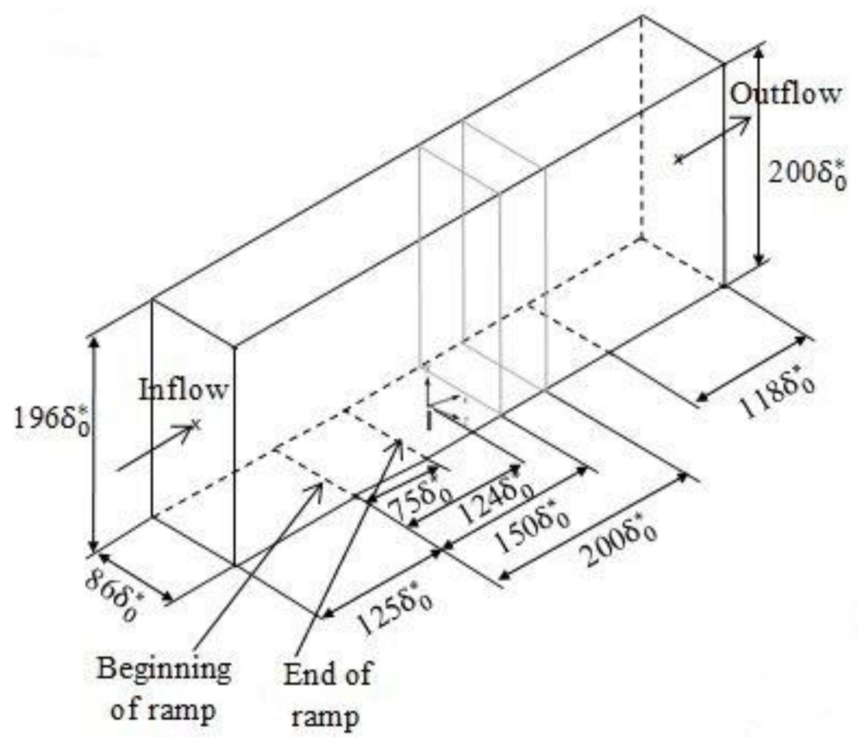

Figure 4.8 Streamwise locations of leading edge, beginning and end of ramp, two streamwise locations where the data is presented in Figures 4.7 and 4.8

Figure 4.8 illustrates the streamwise locations where the datas are presented in Figures 4.9 and 4.10. The spanwise vorticity lines are expected to deform in the streamwise-spanwise plane due to the spanwise non-uniformity of streamwise velo-

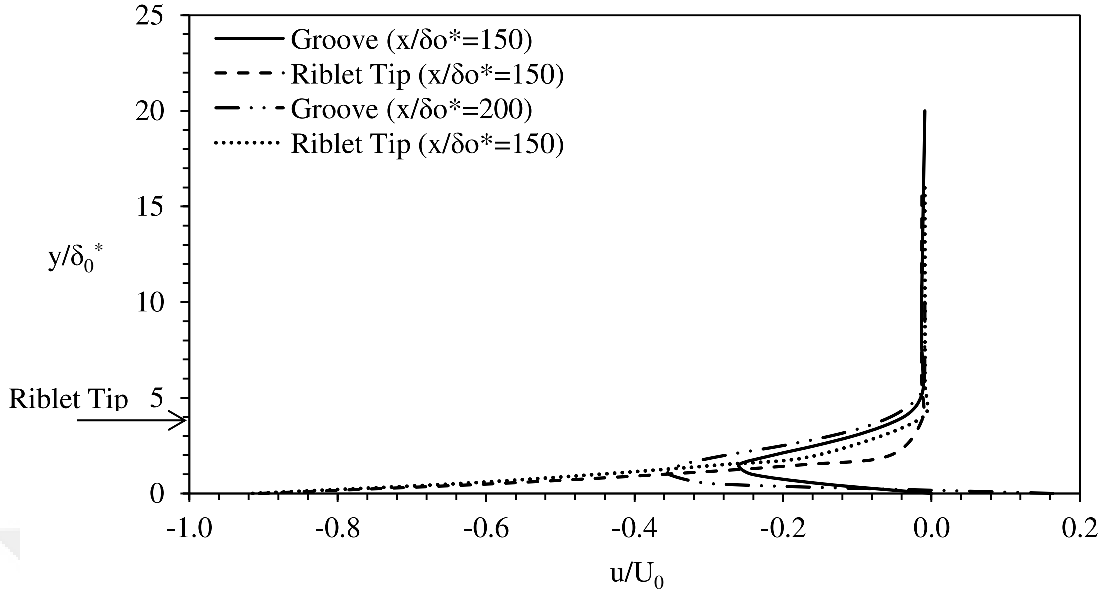

Figure 4.9 Perturbation streamwise velocity over the groove and riblet tip

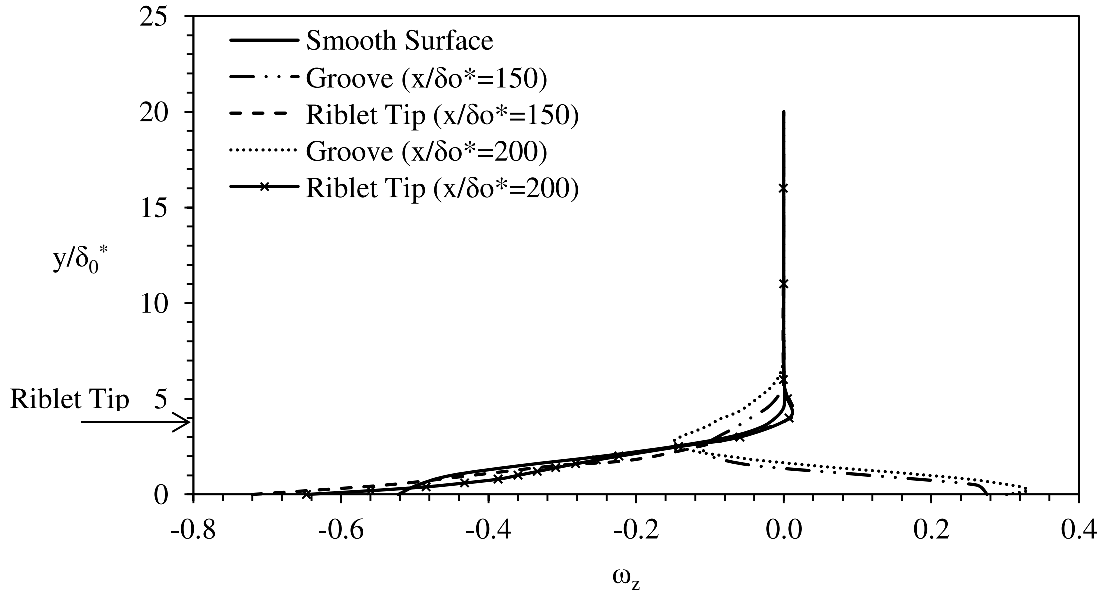

Figure 4.10 Dimensionless spanwise perturbation vorticity over the smooth surface, the groove and riblet tip

city prompted by the presence of the riblets. The effect of the riblets on the spanwise vorticity and streamwise velocity distribution can be readily observed in Figures 4.9 and 4.10. For example, in Figure 4.10, a region of non-zero spanwise vorticity exists within the groove. In addition, the vorticity field in the riblets has a region of increased spanwise vorticity at the inflection point in the streamwise velocity profile from the middle wall-normal position of the groove to the riblet tips.

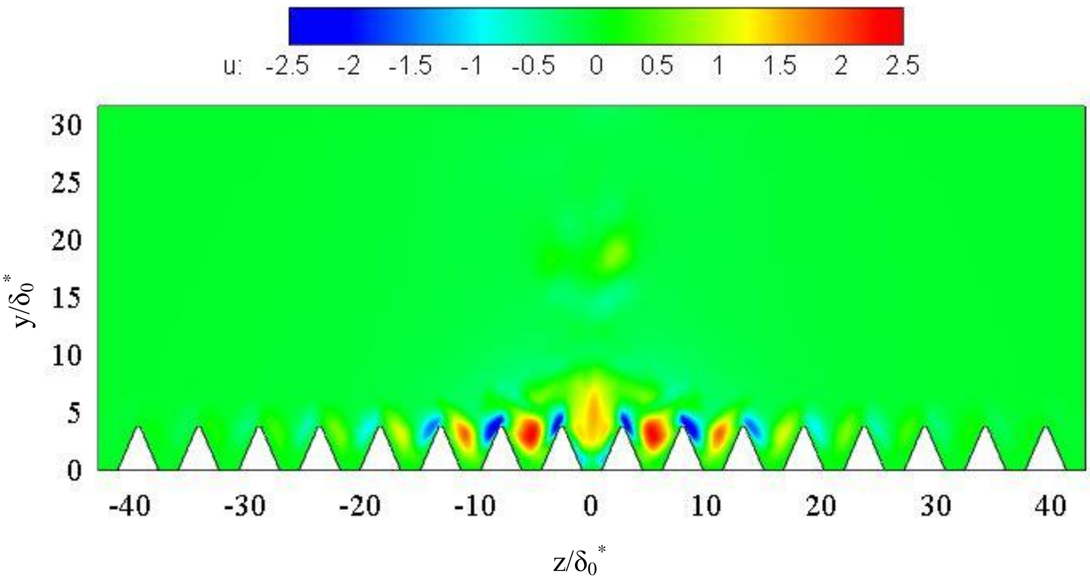

Figure 4.11 Perturbation velocity distribution in the y-z plane at $\tau = 90$

While the low-speed streaks over the riblet surfaces tend to lock onto the position of the riblet tips where they likely reside, the high-speed streaks tend to reside over the grooves as shown in Figure 4.11. This effect results in the control of both the spanwise spacing and the number of low-speed streaks within the spot. One plausible mechanism is the lower streamwise momentum of the fluid in the grooves of the riblet surface that feeds the streaks via the upwash induced by the hairpin vortices straddling the riblet tips. It is expected that the hairpin vortices and correspondingly wave-packets are positioned on the riblet tips as illustrated schematically in Figure 4.12. The present riblets height and spanwise spacings are 75 and 100 wall-units, respectively. These values have a significantly greater influence on the spanwise location of the wave packets than was observed by Goldstein and Tuan (1998) over riblets with a height of 10 wall-units and spanwise spacings of 65.3 wall-units.

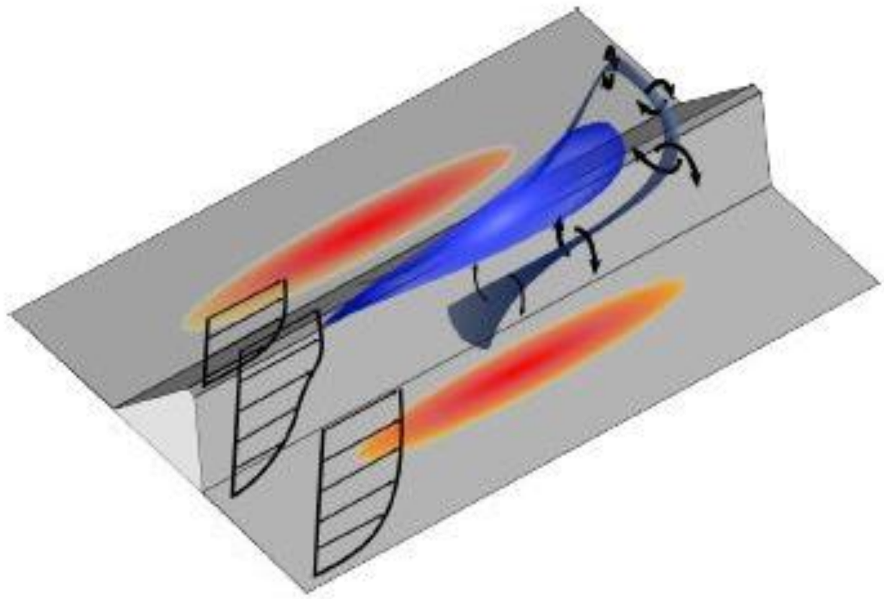

Figure 4.12 Illustration of a hairpin vortex over a single riblet (Adapted from Ancrum and Yaras, 2016)

The riblets tend to have more streaks than the smooth surface over the same spanwise extent. Due to the closer spanwise spacing of the wave packets, an enhancing effect on the turbulent mixing may be possible over the riblets. Some spanwise interaction of hairpin vortices is evident through regions of negative perturbation velocity spanning between adjacent low-speed streaks. These low-speed regions are likely the result of the induced motions of spanwise vortices which form spanning the grooves similar to the observations of Garcia-Mayoral and Jimenez (2011) over riblets spaced 50 wall-units apart. The strength of the spanwise vortices increases greatly with riblet size (Garcia-Mayoral & Jimenez, 2011). Figure 4.9 showed that the riblets could feasibly create strong spanwise vortices which could span the 100 wall unit wide grooves and induce wall-normal motions leading to the observed low-speed regions. The inflection point in the streamwise velocity within the grooves promoted the formation of these spanwise vortices. It is likely that the spanwise vortices forming over the grooves would lock onto the nearby hairpin vortices leading to a bridging of adjacent hairpin vortices. The spanwise vortices forming over the grooves may lead to connect the nearby hairpin vortices each others. The turbulent spot is significantly larger in both the streamwise and spanwise directions than was observed over the smooth surface, because of the combination of increased mutual interaction, the close proximity of the favourable vorticity distribution over the riblets and strengthening of the streak structures.

The larger streamwise dimension of the turbulent spot over the riblet surface compared to the smooth surface is observed to occur as a result of the difference in the leading and trailing edge celerities. The majority of the increase in the streamwise dimension can be accounted for by a significant decrease in the trailing edge celerity of the turbulent spot over the riblet surface. The riblet surface is observed to concentrate the downwash of higher-speed fluid being swept by the streamwise-aligned legs of the hairpin vortices within the riblet groove. The closer spanwise proximity of the hairpin vortices would promote a canceling effect of their spanwise component of induced motion, thus resulting in the concentrated presence of the high-speed streaks with larger perturbation velocity magnitude at the base of the riblet grooves. The riblet grooves prevent dissipation of the high-speed fluid which allows this region to extend well downstream of the spot. The concentrated high-speed streaks, and the reduced streamwise momentum of the fluid within the grooves both contribute to the reduction in trailing edge celerity of the spot. The larger size of the spot can also be attributed to high leading edge celerities compared to the spot over the smooth surface.

CHAPTER FIVE
CONCLUSION

The growth of coherent flow structures over riblet surface in an artificially triggered turbulent spot is studied in this study. The triggering jet that interacts with the riblet test surface boundary layer leads to the formation of coherent flow structures within the spot. The counter-rotating streamwise oriented vortices within the boundary form in the streamwise direction downstream of the jet orifice. A hairpin-vortex regeneration process is activated by these pair of streamwise vortices. The wavepackets consisting of closely spaced, streamwise aligned hairpin vortices form from the new hairpin vortices. Spanwise merging of adjacent hairpin vortices also occurs, leading to an increase in their spatial scale. New wavepackets are repeatedly generated along the spanwise edges of the spot, resulting in lateral growth of the spot.

Two complementary mechanisms are observed about the lateral growth of the turbulent spot. One of them is the regeneration of hairpin vortices within a wavepacket and the other one is the formation of new wavepackets along the spanwise edges of the spot. It is found that the streamwise vorticity between the legs of a parent hairpin vortex activates the regeneration of hairpin vortices within a wavepacket. The downwash motions outboard of the legs and the upwash motions between the legs of the hairpin vortex induced by the streamwise vorticity perturb the spanwise vorticity. Thus, small wall-normal-oriented loops in the boundary layer vorticity adjacent the legs of the parent hairpin vortex can be formed. The shear layers formed by the wall-normal component of the vorticity roll up because of an inviscid instability in the x–z plane, and so the pairs of secondary hairpin vortices straddle a single leg of the parent hairpin vortex. If the legs of parent hairpin vortex are close to each other, the new generation hairpin vortex tends to straddles both legs of the parent hairpin vortex. However, this situation is not observed more frequently.

The riblet surface has an efficient effect in controlling the spanwise positioning of the wavepackets. Notably stronger sweep and ejection events is observed over the riblet surface compared to those with the smooth surface and improved control of the spanwise meandering of the low speed streaks. The riblets promoted the positioning of hairpin vortices over their peaks by changing the spatial distribution of vorticity of the undisturbed laminar boundary layer. This created a locking effect which allowed the spanwise spacing of hairpin vortices to be controlled by the spacing of the riblets. The locking effect of the wavepackets over the riblet peaks led to enhanced stabilization of the low-speed streaks. The riblet surface produced the strongest low-speed streaks due to the low streamwise momentum of the fluid within the grooves which fed the low-speed streaks through the upwash of the hairpin vortex legs. In addition, there is evidence of an additional instability mechanism resulting in the formation of spanwise-oriented vertical structures that interact with the hairpin vortices.

The control of coherent structures within the turbulent spots achieved by the riblet surfaces shows promise as an initial step towards the optimization of these surfaces for different purposes. The closer spanwise spacing of the hairpin vortices over the closer-spaced riblets, their increased mutual interaction, and the resultant increases in the strengths of the low- and high-velocity streaks collectively suggest that the riblets with smaller spacing may have the net effect of promoting turbulence in an organized manner. Whether this can be optimized to realize enhancement in convection heat transfer with only modest increase in skin-friction drag would be worth examining further.

REFERENCES

Adrian, R., Meinhart, C., & Tomkins, C. (2000). *Vortex organization in the outer region of the turbulent boundary layer*. Journal of Fluid Mechanics, *422*, 1-54.

Ancrum, D. B., & Yaras, M. I. (2016). *Measurements of the effects of streamwise riblets on the turbulence structures in boundary layers*. MSc Thesis, Carleton University, Ottawa.

Azih, C., Brinkerhoff, J.R., Yaras, M.I. (2012). *Direct numerical simulation of convective heat transfer in a zero-pressure-gradient boundary layer with supercritical water*. Journal of Thermal Science, *21*, 49-59.

Bechert, D., Bruse, M., Hage, W., der Hoeven, J. V., & Hoppe, G. (1997). *Experiments on drag-reducing surfaces and their optimization with an adjustable geometry*. Journal of Fluid Mechanics, *338*, 59-87.

Boiko, A. (2007). *Effect of riblets on the streaky structures excited by free stream tip vortices in boundary layer*. Journal of Mechanical Science and Technology, *21*, 196-206.

Brandt, L. & Henningson, D. (2002). *Transition of streamwise streaks in zero pressure gradient boundary layers*. Journal of Fluid Mechanics, *472*, 229-61.

Brinkerhoff, J. R. & Yaras, M. I. (2012). *Direct numerical simulation of a square jet ejected transversely into an accelerating, laminar main flow*. Flow Turbulence and Combustion, *89*, 519-546.

Brinkerhoff, J. R. & Yaras, M. I. (2014). *Numerical investigation of the generation and growth of coherent flow structures in a triggered turbulent spot*. Journal of Fluid Mechanics, *759*, 257-294.

Chernorai, V., Kozlov, V., Loefdahl, L., Grek, G., & Chun, H. (2006). *Effect of riblets on nonlinear disturbances in the boundary layer*. Thermophysics and Aeromechanics, *13*(1).

Choi, H., Moin, P., & Kim, J. (1993). *Direct numerical simulation of turbulent flow over riblets.* Journal of Fluid Mechanics, *255*, 503-539.

Choi, H., & Moin, P. (1994). *Effects of the computational time step on numerical solutions of turbulent flow*. J. Comput. Phys., *113*, 1-4.

Chu, D. C., & Karniadakis, G. E. (1993). *A direct numerical simulation of laminar and turbulent flow over riblet-mounted surfaces.* Journal of Fluid Mechanics, *250*, 1-42.

Djenidi, L., & Antonia, R. A. (1993). *LDA measurements in low Reynolds number turbulent boundary layer.* Exp. Fluids, *14*, 280-288.

D'Ovidio, A., Harkins, J. A. and Gostelow, J. P. (2001a). *Turbulent spots in strong adverse pressure gradients Part 1. Spot behavior.* ASME Paper 2001-GT-0194.

D'ovidio, A., Harkins, J. A. and Gostelow, J. P. (2001b). *Turbulent spots in strong adverse pressure gradients Part 2. Spot propagation and spreading rates*. ASME Paper 2001-GT 0406.

Elofsson, A., Kawakami, M., & Alfredsson, P. (1999). *Experiments on the stability of streamwise streaks in plane poiseuille flow*. Physics of Fluids, *11*(1), 915-930.

Emmons, H.W. (1951). *The laminar-turbulent transition in a boundary layer-Part 1*. Journal of Aeronautical Sciences, *18*, 490–498.

Fric, T. F. & Roshko, A. (1994). *Vortical structure in the wake of a transverse jet*. Journal of Fluid Mechanics, *279*, 1–47.

Gad-El-Hak, M., Blackwelder, R. F. and Riley, J. J. (1981). *On the growth of turbulent regions in laminar boundary layers.* Journal of Fluid Mechanics, *110*, 73–95.

Garcia-Mayoral, R. & Jimenez, J. (2011a). *Drag reduction by riblets.* Philosophical transactions: Mathematical, Physical and Engineering Sciences, *369*, 1412-1427.

Garcia-Mayoral, R. & Jimenez, J. (2011b). *Hydrodynamic stability and breakdown of the viscous regime over riblets.* Journal of Fluid Mechanics, *678*, 317-347.

Goldstein, D., Handler, R., & Sirovich, L. (1995). *Direct numerical simulation of turbulent flow over a modelled riblet covered surface.* Journal of Fluid Mechanics, *302*, 333-376.

Goldstein, D. & Tuan, T. (1998). *Secondary flow induced by riblets*. Journal of Fluid Mechanics, *363*, 115-151.

Grek, G. R., Kozlov, V. V., & Titarenko S. V. (1996). *An experimental study of the influence of riblets on transition*. Journal of Fluid Mechanics, *315*, 31-49.

Hama, F. R., Long, J. D. & Hegarty, J. C. (1957). *On transition from laminar to turbulent flow*. Journal of Applied Physics. *28*, 388–394.

Hunt, J. C. R. & Durbin, P. A. (1999). *Perturbed vortical layers and shear sheltering*. Fluid Dynamics Research, *24*, 375.

Johnson, M. (2001). *On the flow structure within a turbulent spot.* International Journal of Heat and Fluid Flow. *22*, 409-416.

Katz, Y., Seifert, A., & Wygnanski, I. (1990). *On the evolution of the turbulent spot in a laminar boundary layer with a favourable pressure gradient*. Journal of Fluid Mechanics, *221*, 1-22.

Kim, J., Kline, S., & Reynolds, W. (1971). *The production of turbulence near a smooth wall in a turbulent boundary layer.* Journal of Fluid Mechanics, *50*, 133–160.

Kim, J., Moin, P., & Moser, R. (1987). *Turbulence statistics in fully developed channel flow at low Reynolds number*. Journal of Fluid Mechanics, *177*, 133-166.

Klebanoff, P. (1971). *Effect of freestream turbulence on the laminar boundary layer.* Bulletin of the American Physical Society, *10*, 1323.

Klewicki, J. C., & Falco, R. E., (1990). *On accurately measuring statistics associated with small-scale structure in turbulent boundary layers using hot-wire probes*. Journal of Fluid Mechanics, *219*, 119-142.

Kline, S. J., Reynolds, W. C., Schraub, F. A., & Runstadler, P. W. (1967). *The structure of turbulent boundary layers*. Journal of Fluid Mechanics, *30*, 741-773.

Klumpp, S., Meinke, M., & Schroder, W. (2010). *Numerical simulation of riblet controlled spatial transition in a zero-pressure-gradient boundary layer*. Flow, Turbulence and Combustion, *85*, 57-71.

Lee, S., & Lee, S. (2001). *Flow field analysis of a turbulent boundary layer over a riblet surface*. Experiments in Fluids, *30*, 153-166.

Mansour, N. N., Kim, J., & Moin, P. (1988). *Reynolds-stress and dissipation-rate budgets in a turbulent channel flow*. Journal of Fluid Mechanics, *194*, 15-44.

Mohammadi, A., Moradi, H. V., & Floryan, J. M. (2015). *New instability mode in a grooved channel.* Journal of Fluid Mechanics, *778*, 691-720.

Moradi, H. V., & Floryan, J. M. (2014). *Stability of flow in a channel with longitudinal grooves.* Journal of Fluid Mechanics, *757*, 613-648.

Morkovin, M. (1969). *On the Many Faces of Transition*. 1–31, Viscous Drag Reduction, Plenum.

Perry, A. E., Lim, T. T. and Teh, E. W. (1981). *A visual study of turbulent spots*. Journal of Fluid Mechanics, *104*, 387–405.

Pope, S. (2000). *Turbulent Flows*. Cambridge University Press, New York.

Reed, H., Saric, W. S. and Arnal, D. (1996). *Linear stability theory applied to boundary layers*. Annual Review of Fluid Mechanics, *28*, 389–428.

Reinink, S. K., & Yaras, M. I. (2014). *Numerical Study of Coherent Structures of Turbulence with Large Wall-Normal Gradients in Thermophysical Properties.* MSc Thesis, Carleton University, Ottawa.

Sabatino, D. R. and Smith, C. R. (2008). *Turbulent spot flow topology and mechanisms for surface heat transfer*. Journal of Fluid Mechanics, *612*, 81–105.

Sankaran, R. and Antonia, R. A. (1988). *Influence of a favourable pressure gradient on the growth of a turbulent spot*. AIAA Journal, *26*, 885–887.

Schlichting, H. (1968). *Boundary Layer Theory*. McGraw-Hill, New York.

Schröder, A. & Kompenhans, J. (2004). *Investigation of a turbulent spot using multi-plane stereo particle image velocimetry.* Experiments in Fluids, *36*, 82-90.

Schröder, A., Geisler, R., Elsinga, G. E., Scarano, F. and Dierksheide, U. (2008). *Investigation of a turbulent spot and a tripped turbulent boundary layer flow using time resolved tomographic PIV.* Experiments in Fluids, *44*, 305–316.

Schubauer, G. B. & Skramstad, H. (1947). *Laminary boundary layer oscillations and transition on a flat plate*. Journal of the Research of the National Bureau of Standards, *38*, 251–292.

Schubauer, G. B. & Klebanoff, P. S. (1956). *Contributions on the mechanics of boundary layer transition*. National Advisory Committee for Aeronautics Report No. 1289.

Singer, B. A. & Joslin, R. D. (1994). *Metamorphosis of a hairpin vortex into a young turbulent spot.* Physics of Fluids, *6*, 3724–3736.

Smith, C. R. & Metzler, S. P. (1983). *The characteristics of low-speed streaks in the near-wall region of a turbulent boundary layer.* Journal of Fluid Mechanics, *129*, 27–54.

Smith, C. R., Walker, J. D. A., Haidari, A. H. and Sobrun, U. (1991). *On the dynamics of near-wall turbulence.* Philosophical Transactions: Physical Sciences and Engineering, *336*, 131–175.

Stanislas, M., Perret, L. & Foucaut, J.-M. (2008). *Vortical structures in the turbulent boundary layer: a possible route to a universal representation*. Journal of Fluid Mechanics, *602*, 327–382.

Suzuki, Y. & Kasagi, N. (1994*). Turbulent drag reduction mechanism above a riblet surface*. AIAA Journal, *32*, 1781-1790.

Swearingen, J. & Blackwelder, R. (1987). *The growth and breakdown of streamwise vortices in the presence of a wall.* Journal of Fluid Mechanics, *182*, 255–290.

Tani, I. and Hama, F. R. (1953). *Some experiments on the effect of a single roughness element on boundary layer transition*. Journal of the Aeronautical Sciences, *20*, 289-290.

Walsh, M. J. (1982). *Turbulent boundary layer drag reduction using riblets*. AIAA, *82*-0169.

Wygnanski, I., Sokolov, M. and Friedman, D. (1976). *On a turbulent 'spot' in a laminar boundary layer*. Journal of Fluid Mechanics, *78*, 785–819.

Yaras, M. I. (2007). *An experimental study of artificially-generated turbulent spots under strong favorable pressure gradients and freestream turbulence.* Journal of Fluids Engineering, *129*, 563–572.

APPENDIX A

Data Analysis Procedures

This appendix briefly describes the data reduction procedures used in the present study. This includes calculation of perturbation quantities, differential and integral flow parameters, and the second invariant of the velocity gradient tensor.

A.1 Perturbation quantities

The perturbation velocity field is calculated by subtracting the undisturbed velocity field, which is obtained from a wall-normal-streamwise plane in the laminar boundary layer, from the instantaneous velocity field:

$$u(x,y,z,t) = U(x,y,z,t) - U(x,y)_{undisturbed}$$

$$v(x,y,z,t) = V(x,y,z,t) - V(x,y)_{undisturbed}$$

$$w(x,y,z,t) = W(x,y,z,t) - W(x,y)_{undisturbed}$$

Components of perturbation vorticity are then calculated directly from components of perturbation velocity:

$$\omega_x = \frac{\partial_w}{\partial_y} - \frac{\partial_v}{\partial_z}$$

$$\omega_y = \frac{\partial_u}{\partial_z} - \frac{\partial_w}{\partial_x}$$

$$\omega_z = \frac{\partial_v}{\partial_x} - \frac{\partial_u}{\partial_y}$$

A.2 Differential Flow Parameters

Differential quantities are computed using a centred-differencing scheme. In the x and z directions, derivatives are evaluated as:

$$\left.\frac{\partial \phi}{\partial x}\right|_i = \frac{\phi_{i+1} - \phi_{i-1}}{x_{i+1} - x_{i-1}}$$

where ϕ is a generic flow variable, i is the node at which the derivative is evaluated, and the derivative is evaluated in the x direction as an example. At nodes along boundaries, first-order forward- or backward-differencing schemes are used as applicable.

Because of large wall-normal gradients in flow parameters and non-uniform node spacing, in the y direction a quadratic curve fit is applied to y_{i-1}, y_i, and y_{i+1}. The derivative is taken of the curve fit and evaluated at y_i to yield the following centred-differencing expression for the derivative at node i:

$$\left.\frac{\partial \phi}{\partial y}\right|_i = \frac{y_i - y_{i+1}}{(y_{i-1} - y_i)(y_{i-1} - y_{i+1})} + \phi_i \frac{2y_i - y_{i-1} - y_{i+1}}{(y_i - y_{i+1})(y_i - y_{i-1})} + \phi_{i+1} \frac{y_i - y_{i-1}}{(y_{i-1} - y_{i+1})(y_i - y_{i+1})}$$

At boundary nodes, derivatives in the y direction are evaluated using the following forward- and backward-differencing expressions, respectively, similar to centred-differencing expression:

$$\left.\frac{\partial \phi}{\partial y}\right|_i = \phi_i \frac{2y_i - y_{i+1} - y_{i+2}}{(y_i - y_{i+1})(y_i - y_{i+2})} + \phi_{i+1} \frac{y_i - y_{i+2}}{(y_{i+1} - y_i)(y_{i+1} - y_{i+2})} + \phi_{i+2} \frac{y_i + y_{i+1}}{(y_i - y_{i+2})(y_{i+1} - y_{i+2})}$$

$$\left.\frac{\partial \phi}{\partial y}\right|_i = \phi_{i-2} \frac{y_i - y_{i-1}}{(y_{i-2} - y_{i-1})(y_{i-2} - y_i)} + \phi_{i-1} \frac{y_i - y_{i-2}}{(y_{i-1} - y_i)(y_{i-1} - y_{i-2})} + \phi_i \frac{2y_i - y_{i-2} - y_{i-1}}{(y_{i-2} - y_i)(y_{i-1} - y_i)}$$

A.3 Identification of coherent vortical structures of turbulence

Coherent vortical structures of turbulence are visualized in the present study using the second invariant of the velocity gradient tensor, denoted Q. Lesieur et al. (2005) define coherent vortical structures of turbulence as regions with a high concentration of vorticity with a low static pressure core, such that the fluid particles rotating about the vortex are relatively balanced between centrifugal and pressure gradient forces. Dubief and Delcayre (2000) and Lesieur et al. (2005) mathematically demonstrate that a necessary condition for the presence of a vortex tube with a low-pressure core is $Q > 0$.

Brinkerhoff (2014) determined that turbulence structures are most clearly visualized when Q is calculated using the perturbation velocity flow field. The perturbation velocity flow field can be expressed as:

$$u = Ax$$

or

$$\begin{pmatrix} u \\ v \\ w \end{pmatrix} = \begin{pmatrix} \frac{\partial u}{\partial x} & \frac{\partial u}{\partial y} & \frac{\partial u}{\partial z} \\ \frac{\partial v}{\partial x} & \frac{\partial v}{\partial y} & \frac{\partial v}{\partial z} \\ \frac{\partial w}{\partial x} & \frac{\partial w}{\partial y} & \frac{\partial w}{\partial z} \end{pmatrix} \begin{pmatrix} x \\ y \\ z \end{pmatrix}$$

where A is the velocity gradient tensor. The second invariant of A is therefore (chong et al., 1990):

$$Q = \begin{vmatrix} \frac{\partial u}{\partial x} & \frac{\partial u}{\partial y} \\ \frac{\partial v}{\partial x} & \frac{\partial v}{\partial y} \end{vmatrix} + \begin{vmatrix} \frac{\partial u}{\partial x} & \frac{\partial u}{\partial z} \\ \frac{\partial w}{\partial x} & \frac{\partial w}{\partial z} \end{vmatrix} + \begin{vmatrix} \frac{\partial v}{\partial y} & \frac{\partial v}{\partial z} \\ \frac{\partial w}{\partial y} & \frac{\partial w}{\partial z} \end{vmatrix}$$

$$Q = \frac{\partial u}{\partial x}\frac{\partial v}{\partial y} - \frac{\partial u}{\partial y}\frac{\partial v}{\partial x} + \frac{\partial u}{\partial x}\frac{\partial w}{\partial z} - \frac{\partial u}{\partial z}\frac{\partial w}{\partial x} + \frac{\partial v}{\partial y}\frac{\partial w}{\partial z} - \frac{\partial v}{\partial z}\frac{\partial w}{\partial y}$$

$$Q = \frac{1}{2}\left(\frac{\partial u_i}{\partial x_i}\frac{\partial u_j}{\partial x_j} - \frac{\partial u_i}{\partial x_j}\frac{\partial u_j}{\partial x_i}\right)$$

APPENDIX B

Nomenclature

C_f : Friction factor = $0.5\ \tau_w/(\rho U_0^2)$

d : Dimension on riblet surface [mm]

DNS : Direct numerical simulation

K : Acceleration parameter $= \frac{\nu}{U_e^2}\frac{dU_e}{dx}$

$K-H$: Kelvin – Helmholtz

$\dot{m}_{\text{norm}}$: Normalized mass flow rate

N_x : Number of nodes in the x direction

N_y : Number of nodes in the y direction

N_z : Number of nodes in the z direction

P : Static pressure [Pa]

P^+ : Turbulence kinetic energy production rate [m^2/s^2]

Q : Second invariant of the velocity gradient tensor

$Re_{\delta_0^*}$: Reynolds number based on displacement thickness at the jet orifice

Re_θ : Reynolds number based on momentum thickness

Re_τ : Reynolds number based on channel half-height

t : Time [s]

t^+ : Normalized time

t_{jet} : Transverse jet duration [ms]

$T-S$: Tollmien – Schlichting

U : Streamwise velocity component [m/s]

u : Streamwise component of perturbation velocity [m/s]

U^+ : Mean velocity profile

u^+ : Streamwise velocity component in wall unit

U_0 : Undisturbed free-stream velocity [m/s]

U_e : Streamwise distribution of the freestream velocity [m/s]

u_j : Instantaneous velocity vector

u_τ : Friction velocity = $\sqrt{\tau_w/\rho}$ [m/s]

V : Wall-normal velocity component [m/s]

w : Perturbation vorticity [1/s]

W : Spanwise velocity component [m/s]

x : Streamwise spatial coordinate

y : Wall-normal spatial coordinate

z : Spanwise spatial coordinate

α-ζ : Coordinate system which is locally parallel to the test surface

β : Groove wavenumber

β_{tran} : critical value of groove wavenumber

δ_0^* : Displacement thickness of the undisturbed boundary layer for the smooth surface [mm]

ε^+ : Turbulence kinetic energy dissipation rate [m^2/s^3]

η : Kolmogorov length scale [mm]

η^+ : Kolmogorov length scale normalized with the viscous length scale, u_τ/ν

θ : Riblet side-wall angle

ν : Kinematic viscosity [m^2/s]

ρ : Density [kg/m^3]

τ : Dimensionless time

τ_{jet} : Normalized jet duration

τ_w : Wall shear stress [kg/ms^2]

ϕ : Generic flow variable

Subscripts

0 : Reference location at test-surface leading edge

i,j,k : Imaginary components of a complex number

jet : Jet-flow condition

rms : Root mean square

w : Wall shear

x : Component in x spatial direction

y : Component in y spatial direction

z : Component in z spatial direction

Superscripts

\+ : Quantity normalized using wall parameters